Assessment of benthic disturbance associated with stingray foraging for ghost shrimp by aerial survey over an intertidal sandflat

Seiji Takeuchi[a], Akio Tamaki[a,*]

a Graduate School of Fisheries Science and Environmental Studies, Nagasaki University, Bunkyo-machi 1-14, Nagasaki 852-8521, Japan

***** Corresponding author. Tel.: +81 95 819 2856; fax: +81 95 819 2799

E-mail address: tamaki@nagasaki-u.ac.jp (A. Tamaki)

Abstract

One notable type of bioturbation in marine soft sediments involves the excavation of large pits and displacement of sediment associated with predator foraging for infaunal benthos. Batoids are among the most powerful excavators, yet their impact on sediment has been poorly studied. For expansive temperate tidal flats, only relatively small proportions of the habitat can be sampled due to physical and logistical constraints. The knowledge of the dynamics of these habitats, including the spatial and temporal distribution of ray bioturbation, thus remains limited. We combined the use of aerial photogrammetry and *in situ* benthic sampling to quantify stingray feeding pits in Tomioka Bay, Amakusa, Japan. Specifically, we mapped newly-formed pits over an 11-ha section of an intertidal sandflat over two consecutive daytime low tides. Pit size and distribution patterns were assumed to scale with fish size and reflect size-specific feeding behaviors, respectively. *In situ* benthic surveys were conducted for sandflat-surface elevation and prey density (callianassid shrimp). The volume versus area relationship was established as a logistic function for pits of varying sizes by photographing and refilling them with sediment. This relationship was applied to the area of every pit detected by air to estimate volume, in which special attention was paid to ray ontogenetic change in space utilization patterns. In total, 18103 new pits were formed per day, with a mean individual area of 1060 cm^2. The pits were divided into six groups (G1 to G6 in increasing areas), with abundances of G1, G2+G3, and G4–G6 being medium, high, and low, respectively. Statistical analyses using generalized linear models revealed a marked preference for the higher prey-density areas in G1 and the restriction of feeding grounds of G4–G6 to the lower shore, with G2+G3 being generalists for prey density and sandflat elevation. The lower degrees of overall bioturbation by G1 and G4–G6 were spatially structured for the eight sub-areas demarcated by prey density and sandflat elevation, while G2+G3 homogenized the state over the sandflat. The newly-formed pits' sub-areal

mean numerical, excavated-areal, and displaced-sediment-volume densities per day were confined to small ranges: 0.14–0.17 m^{-2}, 132–223 cm^2 m^{-2}, and 551–879 cm^3 m^{-2} (latter two including 119 shallow non-pit excavations). These bioturbation rates are positioned at relatively high levels compared with those by rays from other geographic regions. The present procedure is applicable to the assessment of disturbance by any surface-sediment excavators on tidal flats if their pit dimensions are discernible from the air.

***Keywords*:**

bioturbation; stingray; foraging; ghost shrimp; intertidal sandflat; aerial survey

1. Introduction

The excavation of large pits and displacement of corresponding amounts of sediment associated with predator foraging for infaunal macrobenthos or megaherbivore grazing on epibenthic vegetation are classic examples of bioturbation in marine and estuarine soft-sediment habitats (Bromley, 1996; Cadée, 2001; Hall et al., 1994; Meysman et al., 2006). In the marine bioturbator classification, these consumers are regarded as large epifaunal biodiffusors (Kristensen et al., 2012). This group includes vertebrates such as gray whale (Johnson and Nelson, 1984; Weitkamp et al., 1992), walrus (Oliver et al., 1985), sea otter (Hines and Loughlin, 1980), dugong (Preen, 1995; Skilleter et al., 2007), birds (Cadée, 1990; Nacken and Reise, 2000), sea turtle (Lazar et al., 2011) and demersal fish (Howard et al., 1977; Orth, 1975; Yahel et al., 2002), and invertebrates such as horseshoe crab (Botton, 1984; Woodin, 1978) and decapod crabs (Thrush, 1986; Woodin, 1978). The considerable modification of seabed topographies by these organisms is accompanied by sedimentological and biogeochemical

consequences for the ambient environment originally set by current and wave actions, such as sediment and nutrient resuspension into the water column (Johnson and Nelson, 1984; Ray et al., 2006; Yahel et al., 2008; Yahel et al., 2002), detritus accumulation in pits (Hall et al., 1991; VanBlaricom, 1982), lateral transport of displaced sediment (Grant, 1983; Johnson and Nelson, 1984), and vertical mixing of this sediment in the substratum column (D'Andrea et al., 2004).

One major limitation to the assessment of high-magnitude epifaunal biodiffusors' pit formation and concurrent sediment displacement lies in the difficulty to cover a sufficiently large area of the seabed with inherent spatial heterogeneity. Small-scale observations would not necessarily be extrapolated to an unexplored larger area. For predators excavating feeding pits, the "total area" needed for full assessment depends on the availability of information on pit size-frequency distribution, density, local dispersion pattern, and landscape-scale distribution (Hall et al., 1994). Sampling these areas in the field is constrained by low-tide times for intertidal assessments and to scuba limitations for subtidal beds. Thus, these techniques generally cover relatively small proportions of the seabed, between 50 and 26900 m^2 (Cadée, 1990; D'Andrea et al., 2004; Grant, 1983; Hall et al., 1991; Hines et al., 1997; Myrick and Flessa, 1996; Nacken and Reise, 2000; O'Shea et al., 2012; Thrush, 1986; Thrush et al., 1991; VanBlaricom, 1982; Woodin, 1978). Several attempts have been undertaken to cover larger areas. For a 20–40-m deep, 22000-km^2 bed of the northeastern Bering Shelf, side-scan sonar was used to detect feeding excavations by gray whales and walruses (Johnson and Nelson, 1984; Nelson et al., 1987; Ray et al., 2006). Aerial and/or boat-based censuses have also been previously used to map epifaunal bioturbator impacts in shallow subtidal beds with high water clarity. These methods have been applied to vegetation patches resulting from grazing by dugongs in seagrass beds with up to a 110-km^2 area (Preen, 1995) and from cownose ray digging in eelgrass beds up to a 24-ha area (Hovel and Lipcius, 2001; Orth, 1975) and pits formed by stingrays in a 1-km^2 lagoon (O'Shea et al., 2012). Aerial surveys have been least

used for intertidal zones, with only one study of gray whale pits along a 90–180-km stretch of Puget Sound shoreline in Washington, U.S.A. (Weitkamp et al., 1992) and another on horseshoe crab pits by digital camera moving along a 50-m long cable (Lee, 2010).

Of the demersal fish epifaunal biodiffusors in soft-sediment habitats, rays (Chondrichtheyes: Batoidea) are among the most powerful excavators that can make large pits (e.g. 1-m wide and 10s-cm deep) as they prey on deep-dwelling infauna from sandy substrate (Cadée, 2001; Kristensen et al., 2012). Preys are mined hydraulically by jetting water from the mouth or gills (Gregory et al., 1979; Sasko et al., 2006). Prey targeted in these habitats vary among ray taxa; cownose rays and eagle rays generally select bivalve mollusks (Ajemian et al., 2012; Hines et al., 1997; Peterson et al., 2001), while stingrays favor decapod crustaceans and fish (Ebert and Cowley, 2003; Howard et al., 1977; Taniuchi and Shimizu, 1993; Tillett et al., 2008). Some studies suggest that density-dependent foraging behaviors of rays could stabilize local prey populations (Ajemian et al., 2012; Hines et al., 1997) and bring about prey metapopulation source–sink dynamics (Peterson et al., 2001).

Two measures associated with ray pit excavations have been considered as their basic bioturbation rates: (1) numerical density and distribution of newly-formed pits with various horizontal and vertical dimensions and (2) volumetric density and distribution of sediment displaced aside newly-formed pits. To date, only a handful of estimates have been presented for these measures, which were generally extracted from a small portion of each study site (Cross and Curran, 2004; D'Andrea et al., 2004; Grant, 1983; Hines et al., 1997; Myrick and Flessa, 1996; O'Shea et al., 2012; Reidenauer and Thistle, 1981; Sherman et al., 1983; Thrush et al., 1991; Valentine et al., 1994; VanBlaricom, 1982). It is only after the proper assessment of these bioturbation rates that the subsequent processes of lateral transport of discarded sediment and vertical mixing in the substratum column can be evaluated (D'Andrea et al., 2004; Myrick and Flessa, 1996). Aerial methods can be a strategic tool to help enlarge the survey areas that likely contain high spatial heterogeneity in each

habitat type, especially within intertidal zones that have limited access due to tidal activity. The ray bioturbation rates can vary spatially, depending on the physical setting of feeding grounds and the prey-density distribution. Physical components of heterogenetiy in intertidal zones include: thickness of sediment column in which deep-dwelling benthic prey can escape from surface disturbance, and surface topographic elevation. The latter component is particularly relevant to high-tide predators like stingrays, which access this zone from the subtidal region and are thus at risk of being stranded with receding tides. Regarding the influence of prey abundance, only Hines et al. (1997) described a spatially varying prey-density-dependent pit-excavation rates for eagle rays. Finally, for estimating the volume of displaced sediment from pits, semi-ellipsoid or inverted-cone approximation to pit shape has sometimes been made, with circular or elliptical area and maximum depth given (Cross and Curran, 2004; D'Andrea et al., 2004; O'Shea et al., 2012), but more reliable estimates can be obtained by direct refilling of pits (Myrick and Flessa, 1996).

Long-term observations (1979–2001) of the benthic community on an intertidal sandflat in Amakusa-Shimoshima Island, western Kyushu, southern Japan (Fig. 1) indicated an abrupt increase in pits formed by the stingray, *Dasyatis akajei* (Müller & Henle) from 1995 (Flach and Tamaki, 2001; Harada and Tamaki, 2004). Based on a long-term (1972–2001) annual fishery landing record from the four prefectural governments surrounding Ariake Sound adjacent to the present study area, Yamaguchi (2005) summarized trends in the abundance of rays and sharks in the sound: (1) rays increased steadily to reach a maximum during 1988 to 1995 and thereafter decreased to a level which was still higher than those before 1985, (2) *D. akajei* accounted for most of these rays, and (3) sharks decreased largely continuously to 1997, with a subsequent slight increase. In Amakusa, the stingray almost exclusively forages on ghost shrimp (Decapoda: Axiidea: Callianassidae), *Nihonotrypaea harmandi* (Bouvier), the most dominant species in biomass in the benthic community (Flach and Tamaki, 2001; Harada and Tamaki, 2004). In other parts of the world, ghost shrimps

121 co-occur with ray pits in intertidal-flat habitats (D'Andrea et al., 2004; Martinell et al., 2001; Myrick
122 and Flessa, 1996) and are reported to be a major prey item for dasyatid stingrays (Ebert and Cowley,
123 2003; Howard et al., 1977; Tillett et al., 2008). In Amakusa, the decline of the ghost shrimp
124 population occurring since 1995 has been attributed to increased predation pressure by *D. akajei*,
125 which has induced cascading effects on other members of the benthic community (Flach and Tamaki,
126 2001; Harada and Tamaki, 2004; Mandal et al., 2010). A similar chain of events originally caused by
127 *D. akajei* population increase was recently documented for an intertidal sandflat community in
128 Ariake Sound (Takeuchi et al., 2013). However, pit-related bioturbation rates on the sandflat in
129 Amakusa remain to be quantified except for some preliminary data (Harada and Tamaki, 2004); until
130 around 2000, the manual census of stingray feeding pits during low-tide hours was not entirely
131 impossible at least for a narrow strip along tidal gradient. Most recently, this is no longer feasible
132 due to the overwhelming pit density.
133 The first objective of the present study was to construct digitized maps of newly-formed stingray
134 pits over an 11-ha section of the above intertidal sandflat in Amakusa. As the most basic premise of
135 the study, pit size and distribution patterns were assumed to scale with fish size and reflect
136 size-specific feeding behaviors, respectively (Hall et al., 1994; Hines et al., 1997). Following the
137 result of a pilot aerial survey, a main aerial survey over two consecutive daytime low tides was
138 performed to detect pits formed in one day. At the same time, benthic surveys were conducted for
139 sandflat-surface elevation profile, sand-column thickness, and ghost shrimp density. Furthermore,
140 the maximum-depth–area and volume–area relationships were established for pits of varying sizes
141 by photographing excavations and refilling them with measurable quantities of sediment on the
142 ground. These relationships were applied to the area of every pit detected by air to estimate its
143 maximum depth and volume, in which special attention was paid to the stingrays' ontogenetic
144 change in their space utilization pattern with regard to ghost shrimp density and sandflat elevation.

145 Finally, an assessment was made on spatial variation in numerical density, excavated-area density,
146 and estimated displaced-sediment-volume density of pits per day over the sandflat, and the mean
147 values for these bioturbation rates were compared with those obtained or estimated for ray pits from
148 other geographic regions.
149
150 **2. Materials and methods**
151
152 *2.1. Study site and benthic community*
153 The intertidal sandflat is located in a shallow sub-embayment of Tomioka Bay situated on the
154 northwestern corner of Amakusa-Shimoshima Island in western Kyushu, Japan (Tomioka sandflat;
155 130°02′E, 32°31′N; Fig. 1A–C). The sediment of the sandflat is moderately well-sorted fine sand,
156 with 0.3–1.7% silt-clay content (Wardiatno et al., 2003), and with relatively small ripples (Fig. 2B:
157 wave length, 6–11 cm and wave height, 1–1.5 cm; Tamaki, 1984). The waters around Tomioka Bay
158 are under a mesotidal, semidiurnal tidal regime, with the average tidal range of 3 m during spring
159 tides. The sandflat is exposed for a maximum of 150–550 m seaward and 4 km alongshore. Tomioka
160 sandflat faces north–northeast, receiving northerly wind-induced waves from October to May but
161 minimal wave action in the summer months due to prevailing southwesterly winds (Tamaki, 1984,
162 1987). The aerial survey domain was affixed to a 107516-m^2 northwestern edge section of the
163 sandflat with a 540-m alongshore length (Fig. 1D). The water-level change was recorded at a middle
164 point in the domain during the main aerial survey period at a spring tide (17–18 August 2012) using
165 a water-pressure gauge (Wave Hunter 99, IO Technic, Co.; sensor positioned 1.4 cm above the
166 sandflat surface and recorded measurements every 0.5 seconds). To remove any noise associated
167 with very shallow depths, pressure data less than 30 gw cm^{-2} (= 2.94 kPa; hereafter, "gw cm^{-2}" will
168 be used) were eliminated from analysis (see Yamada et al., 2009). The maximum and mean

169 flood-current speeds were 130.7 and 6.1 cm s^{-1} and those for ebb currents were 110.9 and 4.2 cm s^{-1},
170 respectively. The waves were weak, with a significant height of 3.4 cm, which would not have
171 caused rapid changes in the sandflat micro-topography (A. Tamaki, personal observation). The
172 substratum column of the sandflat was composed of 30–60-cm sand portion inhabited by
173 *Nihonotrypaea harmandi*, and a bed of shell (both bivalve and gastropod) remains in the lower layer
174 (Flach and Tamaki, 2001; Tamaki and Ueno, 1998). The shell bed formation could partly be
175 attributed to ghost shrimp biogenic stratification (Myrick and Flessa, 1996; Wardiatno et al., 2003).
176 Since 1979 the change in benthic community has been monitored by A. Tamaki and colleagues twice
177 per year for a 300-m × 300-m northwestern portion of the sandflat, which was included in the
178 present aerial survey domain. During summer, the daytime lowest tides at spring tides take alternate
179 higher and lower levels every two weeks. The main survey time of 2012 was at a higher water level,
180 and the sandflat was exposed for a distance of 240 m seaward. The distance was extended 20–60 m
181 further during the spring tide of the pilot survey time of 2011.

182 In 1979, the *N. harmandi* population occupied the higher one-third zone of the sandflat, and
183 expanded its distribution to encompass the entire intertidal region by 1983 (Tamaki and Ingole,
184 1993). Pits of the stingray, *D. akajei*, rapidly increased in 1995, and have been a persistent
185 topographic feature of the sandflat from June to October in subsequent years, with peak occurrence
186 from the end of June to mid-September; the rays found by enclosing a large portion of the sandflat
187 until its exposure were *D. akajei* only (Harada and Tamaki, 2004; A. Tamaki, unpublished data). The
188 period of occurrence of stingrays coincides with the reproductive season of *N. harmandi*, in which
189 water temperatures are above 20°C (Tamaki et al., 1997).

190

191 *2.2. Stingray foraging characteristics*

192 Previous research for stomach and gut contents of *D. akajei* specimens collected from the

193 Tomioka sandflat has shown that rays from 14 to 60 cm in disc width ingested *N. harmandi* over the
194 full size range of the population from 4 to 42 mm in total length (Harada and Tamaki, 2004). On the
195 sandflat, newly-formed stingray pits are refilled with surrounding sediment usually in 2–5 days,
196 depending on pit size and hydrodynamic conditions (Harada and Tamaki, 2004). Any snapshot of the
197 sandflat surface comprises a mixture of pits with various ages and therefore, to identify the
198 newly-formed pits (i.e. < 1 d), surveys over at least two consecutive dates were required.

199 The stingray pits observed on the Tomioka sandflat can be grouped into two major types: (1) a
200 single semi-ellipsoidal pits (Fig. 2A; Grant, 1983; Howard et al., 1977; Myrick and Flessa, 1996),
201 and (2) a complex of one deep, semi-ellipsoidal pit and an associated shallow, sinuous furrow (Fig.
202 2B). The latter morphology is sometimes found in isolation. These furrow characteristics have not
203 been reported for any other ray species' pits. We supposed that (1) prey search by stingrays initially
204 involved shallow excavations with pectoral fins to form a sinuous furrow and (2) once the target
205 patch was determined, the ray forcefully excavated a deep pit by hydraulically jetting water from its
206 mouth or gills (Gregory et al., 1979; Sasko et al., 2006), leaving a semi-ellipsoidal scar (hereafter
207 termed feeding pit; when either deep, feeding pit or shallow, sinuous furrow alone and their complex
208 are collectively referred to, these are termed foraging traces). We also supposed that isolated sinuous
209 furrows were signs of aborted foraging bouts. The observation that smaller feeding pits were mostly
210 unassociated with sinuous furrows suggests the absence or insignificant force for the initial prey
211 search by smaller stingrays. When approximated to an ellipse on the horizontal plane of the sandflat,
212 the feeding-pit minimum dimensions were ca. 20 cm in long axis and 15 cm in short axis. Any
213 quantitative relationships between depth or volume and area can be used to identify newly-formed
214 foraging traces during manual surveys on the sandflat. Fresh sediment mounds displaced aside
215 feeding pits and sinuous furrows can be another clue for inferring them as newly formed (e.g. signs
216 of lower degrees of sediment dispersal by tidal currents; Fig. 2A,B).

217

218 *2.3. Aerial survey methods and mosaic imaging*

219 Aerial-based detection of newly-formed stingray foraging traces required knowledge of the exact
220 geographic overlap of the corresponding photographs. In August, 2012, we obtained a set of two
221 consecutive dates' color ortho-projected images over the sandflat following standard aerial
222 photogrammetry. The methods employed in the survey are detailed further in the Appendix 1.

223

224 *2.4. Treatment of newly-formed stingray foraging traces on the mosaic images*

225 Tracing the outlines of newly-formed stingray foraging traces on the above-obtained mosaic
226 images was conducted on two displays [Flex Scan SX2762W (27 inch in size) or S2402W (24 inch),
227 EIZO, Co., Ltd.], using GIMP 2.8.2 [http://www.gimp.org/downloads/ (accessed on 9 January 2014)]
228 drawing freeware. The two dates' mosaic images were displayed as separate layers for detecting the
229 newly-formed foraging traces. Due to file-size limitations for practically handling a single image (up
230 to 8 Mb), the mosaic image for each date was divided into 320 sub-images each with 2000 × 2000
231 pixels, using the freeware OpenCV 2.4.1 library [http://opencv.org/ (accessed on 9 January 2014)].
232 The feeding pits and sinuous furrows were recognizable by their darker inside colors (due to the
233 presence of water) than outside and, for large newly-formed pits in particular, by lighter sediment
234 mounds displaced to the side (Fig. 2C–G). The detected newly-formed pits and furrows were
235 displayed in a one-tenth their actual sizes on a new layer, traced, and output as 8-bit RGB color
236 images with the same resolution as in the original mosaic images. Feeding pits and sinuous furrows
237 were discriminated by shape (elliptical versus irregular) and traced separately. The junction between
238 pit and furrow was drawn by smoothly extrapolating from the free part of the feeding pit as an
239 ellipse and closing it (Fig. 2C,E).

240 The area of each feeding pit or sinuous furrow was measured with a freeware, ImageJ 1.46r

241 [http://imagej.nih.gov/ij/ (accessed on 9 January 2014)], in which the total number of 3.24 (=
242 1.8^2)-cm^2 component pixels was enumerated. The measurement error in area for a smallest
243 stingray-pit equivalent was assessed by measuring the area of each of 24 arbitrarily chosen
244 "marker-points" for aerial photogrammetry (for marker points, see Appendix 1 and Fig. 1D; 20-cm ×
245 20-cm square boards were used; 14 from the southern part of the survey area on the first day and 10
246 from the northern part on the second day). For the procedure hereafter, the RGB color image was
247 transformed into an 8-bit gray-scale image with 256 pixel values; the feeding pit and the sinuous
248 furrow were given different specific colors. Then further binarization (1 versus 0) was applied to the
249 feeding pits versus the others and to the sinuous furrows versus the others, respectively. Finally, the
250 members of the feeding-pit group and those of the sinuous-furrow group were labeled respective
251 serial numbers, in which all component pixels of each member were given an identical number. To
252 avoid lumping two feeding pits that were partially touching, the watershed segmentation had
253 beforehand been made for all pits, using Watershed command in ImageJ. The representative
254 geographic coordinate position for each of the feeding pits and sinuous furrows on the ground was
255 defined as the means for all component-pixel positions.
256
257 *2.5. Estimation of volume of sediment displaced by stingray foraging*
258 To estimate the volume of sediment displaced by stingray foraging for each excavated area
259 measured on the aerial ortho-projected images, the volume–area relationships had to be established
260 based on data acquired by hand for feeding pits and sinuous furrows on the sandflat. The direct
261 infilling of these foraging traces was conducted during low tides on eight dates under calm weather
262 and sea conditions in the period from 14 September to 17 October 2012. Previous research has
263 shown that feeding pits tend to deepen with area; for newly-formed pits, the upper and lower
264 envelope curves for the scatter plots of maximum depth (*D*, cm) versus area approximated to an

ellipse in plane shape (A, m^2) are given as $D = 0.7 \times (10^4A)^{0.3}$ (upper; maximum A = 1.79) and $D = 5.0 \times \ln (10^4A) - 35.3$ (lower; maximum A = 2.13) (A. Tamaki et al., unpublished data). The main causes for the generation of a rather wide range in both maximum depth and area are the differences in the time of pit formation within one day with two high tides and in the wave conditions. The above equations can primarily be referred to for the identification of newly-formed pits *in situ*. Finally, a total of 35 newly-formed feeding pits and 17 associated sinuous furrows were selected on the sandflat. For the feeding pits, the lengths of major axis, minor axis, and maximum depth were measured to the first decimal place in cm. For depths of the sinuous furrows, measurements were made on 1–19 points per furrow along the central part of its winding path. The feeding pits and sinuous furrows were photographed from 2 m above, using a digital camera (Optio WG-2, RICOH, Co., Ltd.) secured on the top edge of a reverse L-shaped pole, with the shutter released remotely. The acquisition of ortho-projected images was assured by monitoring a level attached to the vertical part of the pole. At least four markers were arranged along the edge of pits or furrows per image, with a 70-cm long graduated (to 1 cm) staff placed aside as a scale. In the cases in which the sinuous furrow was associated with the feeding pit, their junction was demarcated by several markers. For the larger feeding pit and sinuous furrow complexes (≥ ca. 1.5 m^2 in total area), it was impossible to capture the entire outline within one image. In such cases, the subdivided images were taken. The infilling of feeding pits and sinuous furrows was conducted separately, into which nearby sediment was poured with measuring cups. The sediment lumps put inside the pit and the furrow were leveled off with a trowel to be finally flush with the surrounding sandflat surface, when the sum total volume was determined to 100 cm^3.

In the laboratory, the above-treated subdivided images were combined into one image on the computer display, automatically with a freeware, Microsoft Image Composite Editor 1.4.4.0 [http://research.microsoft.com/en-us/um/redmond/groups/ivm/ice/ (accessed on 9 January 2014)] or

289 manually with Microsoft Office PowerPoint 2007. Each feeding pit and sinuous furrow was traced
290 along its outline, divided into pixels, and measured for area with reference to the scale staff, using
291 ImageJ. For the feeding pits, maximum depth or volume was regressed against area using linear,
292 power, and logistic models, of which the best-fit ones were selected based on Akaike's Information
293 Criterion (AIC; Akaike, 1973). For the sinuous furrows, a similar analysis was made on
294 volume–area relationship. These regression equations were used to estimate the maximum depth and
295 the volume for all area-measured newly-formed pits and sinuous furrows that had been identified by
296 comparing the two dates' aerial mosaic images.

297 The spatial variation in the numerical, areal, and volumetric densities of the newly-formed
298 stingray foraging traces over the sandflat was examined using 10-m × 10-m unit grid cells. The
299 entire area of the aerial survey was divided into 934 complete cells and 267 irregular-shaped
300 marginal cells (polygons). The smallest marginal cells with area < 1 m^2 (N = 14) were excluded from
301 analysis, as they could bring about extremely high numerical density values when converted to the
302 100-m^2 unit [e.g. 292.1 for a 0.34-m^2 marginal cell versus 59.0 (maximum) and 17.1 ± 7.3 (mean ±
303 SD) for all complete cells; the latter two values for all complete cells and those remaining marginal
304 cells inclusive were 59.0 and 16.5 ± 8.4, N = 1187]. For each cell, the densities of the excavated area
305 (cm^2 m^{-2}) and displaced-sediment volume (cm^3 m^{-2}) were calculated by summing the values for all
306 feeding pits and sinuous furrows that were contained there. For graphic representations, the densities
307 were classed by either Quantile or Natural Breakes (Jenks) modes, using Quantum GIS 1.8.0
308 (Quantum GIS Development Team, 2012).

309

310 *2.6. Numerical density of ghost shrimps and sand-column thickness on the sandflat*

311 Ghost shrimp density was surveyed over the sandflat during low tides on 30 June and 1 July
312 2011 (at 120 points in total), 3 and 4 July 2012 (138 points), and 21 and 24 July 2013 (39 points),

313 with concomitant measurement of sand-column thickness conducted in 2012. The positions of the
314 survey points were recorded with hand-held GPSs (Global Positioning Systems, eTrex Venture HC
315 and Geko 201, Garmin, Co., Ltd.). The ghost shrimp density at each point was estimated based on
316 burrow-opening counts in two 50-cm × 50-cm plots, as a single individual of *N. harmandi* dwells in
317 a Y-shaped burrow with two surface openings (Tamaki and Ueno, 1998). The plots at each point
318 were chosen haphazardly from a relatively flat part of the nearby sandflat surface, with areas
319 showing apparent signs of recent excavations avoided. The sand-column thickness was measured
320 through the above-ground length of a 120-cm long stiff rod (10-mm φ) which was penetrated into
321 the sediment to its basal shell bed. In the laboratory, geostatistical analyses for the above parameters
322 were performed using "R" (R Core Team, 2012). The minimum area that covers all survey points for
323 spatial interpolation (= convex hull) was determined using "chull" function. The convex hull was
324 divided into 2-m × 2-m unit grid cells with each representative point positioned at its center. The
325 values of ghost shrimp density and sand-column thickness for all cells were interpolated following
326 the ordinary Kriging, in which the variogram model was constructed using "variofit" function in
327 "geoR" package (Ribeiro and Diggle, 2001) and the interpolation made using "krige.conv" function.
328 In "variofit" function, "gaussian" was adopted as the "cov.model" argument.
329
330 *2.7. Difference in foraging ranges by stingray size*
331 To characterize foraging ranges by stingrays of the different size groups on the sandflat, a fixed
332 kernel method (Worton, 1989) used for home range analysis in biotelemetry research (e.g. Beisiegel
333 and Mantovani, 2006; Villegas-Ríos et al., 2013) was applied to the 2012 aerial-survey data set on
334 feeding-pit geographic coordinates. In the present study, by "home range" is meant the spatial extent
335 of the main feeding-pit distribution range for each size group, and the 50% home range (core home
336 range) and 95% home range (home range extent) were estimated. This home range is different from

337 that in its ordinary usage [see Cartamil et al. (2003) and Tilley et al. (2013) for stingray examples],
338 but the technique is applicable to the present case. The feeding pits were divided into six groups
339 according to their areal ranges [G1 (= Group 1)–G6; see Section 3.3]. The determination of the two
340 home ranges was made using “getverticeshr” function in “adehabitat” package (Calenge, 2006) run
341 in “R” (R Core Team, 2012), with “lev” arguments in the function set at 50 or 95.
342
343 *2.8. Difference in foraging sites by stingray size according to prey density and sandflat elevation*
344 To detect any selectivity of stingrays of the different size groups (as reflected on the G1–G6 in
345 their pit areas) for prey (ghost shrimp) density and/or sandflat elevation, a generalized linear model
346 (GLM) fitting was performed using “R” (R Core Team, 2012). A random-point data set was made
347 against the 2012 data set of all observed points (throughout G1–G6) in the (x, y)-geographic
348 coordinate. The observed points, with respective feeding-pit areas, were labeled the serial numbers.
349 Using “csr” function in “splancs” package [http://CRAN.R-project.org/package=splancs (accessed
350 on 9 January 2014)], a set of completely random points was generated, with their total numbers the
351 same as for the observed points. Any random point with its serial number identical to that of a
352 specific observed point was assigned the same Gn. The random-point data set in the coordinate for
353 each of the G1–G6 was used as the case for no selections for ghost shrimp density and/or sandflat
354 elevation by stingrays. The ghost shrimp density and sandflat elevation at each observed feeding-pit
355 point and random point were read from the result of the Kriging interpolation for the shrimp-density
356 record in 2012 and the digital elevation model (DEM; see Appendix 1 for details), respectively,
357 using “overlay” function in “sp” package (Pebesma, 2004). The original DEM was modified into a
358 2-m mesh model, which was coarser in spatial resolution but sufficient for the present analysis. The
359 spatial range for the ghost-shrimp density census was shorter by ca. 90 m in alongshore length than
360 in the aerial survey range, and the analysis was made for their overlapped part.

361 In the GLM fitting procedure for each of the G1–G6, the explanatory variables were prey density
362 and sandflat elevation, and the binary response variable was set to take the values of 1 for the
363 observed points and 0 for the random points. The value of the response variable at any point on the
364 geographic coordinate indicates the probability for this point to be a feeding pit. Four GLMs were fit
365 to the response variable, with prey density alone (Model 1), sandflat elevation alone (Model 2), both
366 (Model 3), and null (= indifferent to both; Model 4) used as explanatory variables, assuming a
367 binomial probability distribution for each. The best-fit model was selected based on AIC. The fitness
368 of the models can vary according to random-number sets which are generated differently from run to
369 run in "csr" function. Thus, to examine which of the four models had the highest probability of
370 occurrence as best fit, the generation of random points and subsequent model selection was repeated
371 99 times.
372
373 *2.9. Pilot aerial survey methods and mosaic imaging*
374 A pilot survey with the use of an unmanned helicopter was conducted to confirm the detectability
375 of stingray foraging traces by aerial photography on 31 July 2011 under sunny and calm conditions.
376 A result of this survey was used here to fill a gap of data on stingray foraging traces on the lowest
377 shore that was not covered in the 2012 aerial survey [i.e. between the seaward edge of the white part
378 and the blue line (mean low water level at spring tides) in Fig. 1D]. The methods employed in the
379 survey are detailed further in the Appendix 2.
380 In the laboratory image processing, the whole sandflat was divided into 23 sub-areas each with
381 ca. 95 m in alongshore length × ca. 65 m in shore-normal length. For each sub-area, the component
382 images were combined into one image, using "photomerge" function of an image editor (Photoshop
383 CS4 11.0, Adobe Systems, Inc.), over which a lattice of longitudes and latitudes to the second was
384 drawn based on the predetermined GPS-position data fed into the helicopter. The combined images

were incorporated into a personal computer using Quantum GIS 1.8.0. A total of 55 20-m-diameter circles were randomly scattered over the sandflat and all feeding pits contained in them traced on the display. The measurement error in area for a smallest stingray-pit equivalent was assessed by measuring the area of each of 22 15-cm × 15-cm square marker points (see Appendix 2).

3. Results

3.1. Environmental characteristics and ghost shrimp distribution over the sandflat

The water pressures recorded at the cross-marked point on the sandflat (Fig. 1D) between 17 and 18 August 2012 were converted into the water-column heights by a factor of Δ1 cm in height to Δ1.031 gw cm^{-2} in pressure under the overlying water with a mean practical-salinity-unit value of 31 for August (A. Tamaki, unpublished data). The highest tides with nearly the same water-column heights (ca. 2.7 m) occurred at 20:23 on Day 1 and 08:11 on Day 2. The diurnal inequality was found for the lowest tides, with the nighttime water-column height of 0.4 m at 02:21 on Day 2 (sunset at 19:02; sunrise at 05:46). Between the daytime lowest-tide times on both dates, the continuous submergence duration in the first tide was 11.3 hours and that in the second tide 10.6 hours.

The surface elevation contours (DEM) of the sandflat did not form a zonation pattern parallel with the upper and lower shorelines but consisted of a mosaic of high and low profiles (Fig. 3A). Around the southeastern part of the sandflat, a large area of the higher surface with > 0.56 m in elevation extended from the uppermost shore seaward pointing toward the westernmost breakwater (Fig. 3B, Area I). Toward the northwestern half of the sandflat, Area I connected with zones of the same elevations on the upper shore, which comprised the wider one (Area II) and the narrower fragmented ones along the uppermost shoreline (Area III). The lower surface with ≤ 0.56 m in elevation occupied a wide seaward zone in the northwestern half of the sandflat (Area IV). At its

409 northern periphery, a very narrow extension ran counterclockwise to connect with a wider belt at the
410 same lower elevations between Areas II and III (Area V). On the lowest shore, Area VI and Area VII
411 lay seaward of Area I and Area IV, respectively; Area VII was outside the 2012 aerial survey domain.
412 The continual submergence durations between the daytime lowest-tide times on Days 1 and 2 at
413 points other than the above-mentioned cross-marked point on the sandflat were estimated separately
414 for the first and second tides and their isopleths over the sandflat drawn (Fig. 3C,D). For this
415 procedure, (1) using "smooth.spline" function in "R" (R Core Team, 2012), spline interpolation was
416 made to obtain a complete curve for water-level variation through time at the cross-marked point, in
417 which the values were standardized to the mean sea level at the nearby tide gauge station (Fig. 1D)
418 and (2) the submergence duration at any point was estimated by taking into account the difference in
419 elevation from the cross-marked point on the DEM (Fig. 3A). The color gradation pattern in the
420 first-tide submergence duration was similar to that in the elevation contour (Fig. 3C), with 11–12.4
421 hours on the lower shore and 8–10 hours on the uppermost shore. In the second tide, the lower shore
422 was submerged less than in the first tide by 0.7 hours (Fig. 3D).
423 The sand-column thicknesses over the sandflat ranged from 9 to 120 cm, with mean ± SD [*N*
424 (number of points) = 137] being 47.2 ± 19.9 cm (Fig. 3E). The Kriging interpolation found the
425 thickest columns (around 100 cm) in the northwestern part of Areas II and V and the thinnest
426 columns (around 30 cm) in Area IV. The latter area was generally encircled with gradually thicker
427 sand columns outward. The thinnest columns also occupied a substantial part of the uppermost
428 sandflat.
429 The numerical densities of *N. harmandi* (mean ± SD inds. and maximum m^{-2}, *N*: number of
430 points) were 103.5 ± 65.2 and 268 (*N* = 120) in 2011, 123.3 ± 50.4 and 351 (*N* = 138) in 2012, and
431 134.3 ± 62.6 and 343 (*N* = 39) in 2013 (Fig. 3F–H). In 2011 and 2013, the lowest-shrimp-density
432 area coincided with Area IV, with the lowest elevations and thinnest sand columns (Fig. 3A,E). This

area was generally encircled with gradually higher-density areas outward. The small, highest-density patch occurred in Area V with the thickest sand columns. In 2012, the lowest-shrimp-density area shrank into three separate patches, while the second lowest-density area expanded especially toward the uppermost shore.

3.2. Dimensions of stingray foraging traces based on manual survey on the sandflat

The ranges for the three dimensions of the stingray foraging traces that were measured manually over the sandflat were: (1) feeding pits [*N* (number of samples) = 35]: 3.4–20.4 cm in maximum depth, 243–8898 cm^2 in area, and 270–57200 cm^3 in volume; and (2) associated sinuous furrows (*N* = 17): 2.8–6.0 cm in mean depth, 510–52543 cm^2 in area, and 1140–54600 cm^3 in volume. In the feeding pits, maximum depth deepened with area, and the best-fit model between two variables was expressed as a power function, which was nearly of the same form with the upper one of the two previously known functions over an areal range beyond the maximum value in 2012 (Fig. 4A, solid curve and upper broken curve). This indicates that largely in the present manual survey, the newest group of the feeding pits formed within one day was selected (i.e. ones formed during the second high tide). For sinuous furrows, their mean depths varied little, with grand mean ± SD (*N* = 124) being 4.2 ± 1.7 cm (Fig. 4B). The best-fit models between volume and area were expressed as a logistic function for the feeding pit and as a power function for the sinuous furrow (Fig. 4C,D). Since the regression curve for the feeding pit reached an asymptotic value at around the maximum area, the estimation of volume for the areas beyond 1.0 m^2 would likely to be made with minimal errors.

3.3. Distribution and abundance of stingray foraging traces on the sandflat based on aerial surveys

The measurement error in area for a smallest stingray-pit equivalent was assessed as 0.047 ±

457 0.004 m^2 (mean ± SD, number of markers = 24) against 0.04 m^2 of each marker area. The individual
458 areas of the newly-formed stingray feeding pits that were detected by the aerial survey over the
459 sandflat in 2012 ranged from 243 to 17700 cm^2, with mean ± SD being 1060 ± 816 cm^2 (total
460 number of pits = 18103). The area (*A*, cm^2)-frequency distribution was divided into six groups (Fig.
461 5A, G1–G6): G1 with $A \leq 500$ and *N* (number of pits) = 3159 (17.45% of the total number); G2 with
462 $500 < A \leq 1000$ and *N* = 7397 (40.86%); G3 with $1000 < A \leq 2000$ and *N* = 6275 (34.66%); G4 with
463 $2000 < A \leq 4000$ and *N* = 1066 (5.89%); G5 with $4000 < A \leq 6000$ and *N* = 136 (0.75%); and G6
464 with $A > 6000$ and *N* = 70 (0.39%). The mean ± SD values in *A* from G1 to G6 in order were: 383 ±
465 72, 744 ± 141, 1353 ± 258, 2573 ± 497, 4788 ± 546, and 8383 ± 2250. To give a reference measure,
466 the pits are transformed into circles in shape, with the original areal boundaries and means for these
467 groups converted into the diameter boundaries and means (*DB* and *DM*, cm): G1 ($DB \leq 25$; *DM* =
468 22), G2 ($25 < DB \leq 36$; 31), G3 ($36 < DB \leq 50$; 41.5), G4 ($50 < DB \leq 71$; 57), G5 ($71 < DB \leq 87$; 78),
469 and G6 ($DB > 87$; 103). The minimum, maximum, and grand mean diameters were 17.6, 150.1, and
470 36.7 cm, respectively. The feeding pits were distributed widely over the sandflat, with the larger ones
471 centered on Area IV (Fig. 6A). The mean ± SD and maximum numerical densities of all feeding pits
472 inclusive were 16.5 ± 8.4 and 59.0 pits per 100 m^2, respectively (number of 10-m × 10-m grid cells =
473 1187).

474 The individual sinuous-furrow areas ranged from 865 to 82059 cm^2, with mean ± SD being
475 18475 ± 15988 cm^2 (total number of furrows = 119), in which 91 furrows were associated with
476 feeding pits (Fig. 5B). Almost all feeding pits accompanying sinuous furrows (96%) were over 2500
477 cm^2 in their individual areas (Fig. 5C), which belong to the feeding-pit groups G4–G6 (Fig. 5A). A
478 weak positive correlation was detected between sinuous-furrow and feeding-pit areas ($r = 0.26$; $P <$
479 0.05; Fig. 5D). The sinuous furrows were distributed mainly in Area IV (Fig. 6B; number = 73), in
480 which the mean ± SD and maximum numerical densities were 0.3 ± 1.0 and 13.6 furrows per 100 m^2

481 (number of cells = 280). The mean ± SD numerical densities over the sandflat were 0.1 ± 0.6 100
482 m^{-2} (number of cells = 1187).

483 The 95% kernel home ranges of feeding pits covered most to almost all of the sandflat in all G*n*s
484 (from G1 to G6 in order: nearly 100, 99, 95, 93, 82, and 69% in area), while a successive
485 ontogenetic change was observed for the 50% kernel home ranges (Fig. 7). The position of the
486 largest area of each G*n* shifted gradually from the southeast, through the northwest, to the northeast.
487 The area shrank markedly from G1–G3 (42.2–48.1%) to G4–G6 (19.3–33.6%).

488 In the GLM fitting to test for the selectivity of stingrays of each size group for prey (ghost
489 shrimp) density and/or sandflat elevation (Table 1; Fig. 8), the highest frequencies of the best-fit
490 model among all runs were recorded for Model 3 in G1, G2, G4, and G6, and for Model 2 in G3.
491 Model 1 was slightly more frequent than Model 3 in G5, and Model 4 was never adopted in all G*n*s.
492 The smallest stingrays (G1) showed a strong selectivity for areas with higher prey densities over a
493 wide elevation range, while the largest ones (G6) for areas with lower elevations and lower prey
494 densities. An ontogenetic transition was found between these two groups. Although the best-fit
495 models were different between G2 and G3, their overall graphic shapes depicted a similar pattern,
496 with only weak selectivities for higher prey densities largely irrespective of the elevation. A marked
497 shift in the foraging pattern took place at G4, with a strong selectivity for lower elevations over a
498 wide prey-density range. This tendency was followed by G5. This finding raised the question as to
499 whether the larger stingrays (G4–G6) might utilize the lowest sandflat with the higher prey densities
500 (Area VII) than in Area IV (Fig. 3A,B,G), which was unanswerable from the 2012 survey result due
501 to the submergence of Area VII. This was examined by comparing the distribution of feeding pits
502 with ≥ 0.25 m^2 in area between the 2011 and 2012 aerial surveys (Figs. 5A,C and 9A,B; 2011 data
503 included the older pits); the measurement error in area for a smallest stingray-pit equivalent in 2011
504 was assessed as 0.0308 ± 0.0055 m^2 (mean ± SD, number of markers = 22) against 0.0225 m^2 of

505 each marker area. In 2012, the mean ± SD number of these pits per 100 m^2 over the aerial survey
506 domain was 1.9 ± 1.5 (number of grid cells = 1187). The distribution patterns of those pits in that
507 domain were similar between the two years. In 2011, the mean ± SD numerical densities were
508 significantly higher in Area VII than in Area IV (3.2 ± 1.1 versus 2.3 ± 1.8 100 m^{-2} as converted
509 from the densities per 20-m-diameter circle area; $P < 0.05$ in Mann-Whitney *U*-test for medians;
510 number of circles = 11 for both). Thus, the larger stingrays foraged throughout the lower sandflat,
511 within which they might slightly more utilize the sub-area on the lowest zone with higher prey
512 densities.
513
514 *3.4. Distribution pattern of stingray bioturbation rates over the sandflat*
515 In 2012, the mean ± SD and maximum stingray-excavated-area densities based on those values
516 for the 10-m × 10-m unit grid cells over the 107516-m^2 sandflat were 194 ± 147 (*N* = 1187) and
517 1553 cm^2 m^{-2} (Fig. 10A). Applying the regression equations of the individual displaced-sediment
518 volume versus excavated area for the feeding pit and sinuous furrow (Fig. 4C,D) to their
519 excavated-area densities, the mean ± SD and maximum displaced-sediment-volume densities were
520 estimated at 786 ± 560 (*N* = 1187) and 9399 cm^3 m^{-2} (Fig. 10B). It is estimated that collectively, a
521 total of ca. 86-m^3 sediment was displaced over the sandflat in one day. The vulnerability of prey
522 (ghost shrimps) to sediment excavation by stingrays might rather depend on the latter's feeding-pit
523 depth relative to the sand-column thickness, as the lower portion of the sand column could be a
524 refuge for deep-dwelling infauna. Applying the regression equation of the individual maximum
525 depth versus excavated area for the feeding pit (Fig. 4A) to respective feeding-pit areas in the 2012
526 aerial survey, the maximum depth was estimated for every feeding pit and its proportional depth to
527 sand-column thickness there (Fig. 3E) calculated and plotted over the sandflat (Fig. 10C–F). The
528 widest area in the higher-proportion groups (> 30%) coincided with Area IV, which had the thinnest

529 sand columns. In particular, the pits with > 50% proportion mainly existed there, where the lowest
530 prey-density plots and the two largest pits (G5, G6) were concentrated (Figs. 3F–H and 7E,F).
531 The spatial variation in stingray excavated-area density and displaced-sediment-volume density
532 over the sandflat in 2012 was examined for its sub-areas as classified by the combination of sandflat
533 elevation and prey density that were estimated from the ordinary Kriging interpolations (Fig. 3A,G).
534 Here, each of the elevation and density ranges was equally divided into three classes (mean ± SD
535 given in parenthesis): (1) elevation (m): 0.34 ≤ low (0.45 ± 0.09) < 0.61, 0.61 ≤ mid (0.73 ± 0.07) <
536 0.88 , and 0.88 ≤ high (0.94 ± 0.04) ≤ 1.15; and (2) ghost shrimp density (number of inds. m^{-2}): 28.6
537 ≤ low (89.0 ± 15.8) < 107.82, 107.82 ≤ medium (132.9 ± 20.5) < 187.01, and 187.01 ≤ high (206.0 ±
538 18.0) ≤ 266.20. During the aerial survey period in 2012, the mean water levels in the low- and
539 high-elevation sub-areas at the high tides were 2.6 m and 2.1 m, respectively (each equal for the first
540 and second high tides). Those values at the night lowest tide were 0.3 m and 0 m (= exposed). The
541 nine possible sub-areas comprised discrete patches of a collection of unit grid cells (Fig. 11A): SA1
542 (low elevation; low prey density), SA2 (low; medium), SA3 (low; high), SA4 (mid; low), SA5 (mid;
543 medium), SA6 (mid; high), SA7 (high; low), and SA8 (high; medium); SA9 (high; high) was
544 non-existent. SA1, SA2, SA4, and SA5 together accounted for 86.9% of the whole sandflat area (Fig.
545 11B). Based on the sum total area of each SA and on the excavated-area and
546 displaced-sediment-volume densities for each grid cell (Fig. 10A,B), the sum totals for excavated
547 area and displaced-sediment volume were estimated for each SA (Fig. 11C,D). The mean densities of
548 excavated area and of displaced-sediment volume per square meter were used as the
549 sub-area-specific measures for the degree of stingray bioturbation rates per day. The highest degree
550 of rates was found for SA1 (276.9 cm^2 m^{-2} and 1058.9 cm^3 m^{-2}; Fig. 11E,F), while the lowest values
551 were about half, respectively (126.1 cm^2 m^{-2} and 537.2 cm^3 m^{-2} for SA8). The mean ± SD values for
552 the SA1–6 inclusive (higher group) and SAs 7 and 8 inclusive (lower group; mean only) were 223.0

553 ± 33.0 and 132.1 cm^2 m^{-2} in excavated-area density, and 878.6 ± 126.1 and 550.7 cm^3 m^{-2} in
554 displaced-sediment-volume density, respectively. The lower degree of bioturbation rates in the
555 higher-elevation areas (SA7,8) was due to the absence or very low contributions of G4–G6 and SF
556 (sinuous furrow). The proportional contribution of G1 increased with prey density in each of SA1–3,
557 SA4–6, and SA7,8 groups. Through all sub-area groups, the highest contributions were made by the
558 intermediate feeding-pit-size groups (G2,G3) which were most abundant in the stingray population
559 (Fig. 5A). For excavated-area density, the ranges in percentage contribution of G1, G2+G3, and
560 (G4–G6)+SF, with their sub-areas where each edge value was found given in parenthesis, were:
561 3.3% (SA1)–9.0% (SA8), 48.6% (SA1)–89.3% (SA7), and 5.9% (SA7)–48.1% (SA1), respectively.
562 Those values for displaced-sediment-volume density were: 5.2% (SA1)–12.5% (SA8), 49.6%
563 (SA1)–86.3% (SA7), and 7.0% (SA7)–45.2% (SA1), respectively.
564
565 **4. Discussion**
566
567 In spite of wide recognition of rays as a prominent epifaunal biodiffusor of estuarine and coastal
568 soft sediments (Cadée, 2001; Hall et al., 1994; Kristensen et al., 2012), quantitative measurement or
569 estimation of their sediment excavation rates has been limited. On the Tomioka sandflat, foraging
570 traces of *D. akajei* became numerous rather abruptly from 1995 (Harada and Tamaki, 2004), which
571 has prompted us to undertake a proper assessment of their bioturbation rates. It is suspected that the
572 proliferation of stingray foraging traces on the sandflat might be related to a recent trend in
573 population increases in some rays and small-bodied sharks occurring in estuarine and coastal waters
574 over a wide geographic range (Heithaus et al., 2010; Myers et al., 2007). These authors' view of
575 meso-predator release following the decline of large-bodied sharks (apex predators) might explain
576 the opposite fishery landing trends between rays and sharks in Ariake Sound, as summarized in

577 Yamaguchi (2005). Intertidal sandflats in the estuarine and coastal waters of western Kyushu appear
578 to have entered a new regime characterized by intense stingray excavations during the late spring to
579 mid-autumn months (Harada and Tamaki, 2004; Takeuchi et al., 2013). In particular, north-facing
580 sandflats in the region become subjected to chronic disturbances throughout the year, as they
581 normally receive seasonal wind-induced waves during mid-autumn to mid-spring (Tamaki, 1987).
582 How foraging sites are selected by predators affects prey population structure and sediment
583 bioturbation (Hall et al., 1994). The prey-density-dependent foraging pattern has been demonstrated
584 for a limited number of species of rays from shallow embayment or lagoon waters. In the subtidal
585 habitats, the predation impact on the local prey population was devastating (Peterson et al., 2001) or
586 modest (Ajemian et al., 2012). To our knowledge, Hines et al. (1997) is the only other study that
587 provides a detailed description of rays' prey-patch use for tidal-flat habitats. The foraging activity of
588 eagle rays (*Myliobatis tenuicaudatus*) was low and independent of infaunal bivalve prey densities
589 but increased linearly beyond a threshold density, not reaching satiation. This could lead to the
590 leveling off the bivalve density over the survey area as rays preferentially forage in high density
591 patches and thus smooth gradients. This total survey area was 12.5 ha in which both ray feeding-pit
592 and bivalve densities were censused manually for the ca. 1/5 subset areas and extrapolated to the
593 whole. The total area in the present study (11 ha) is nearly equivalent to the above value, with the
594 aerial survey enabling analysis for the entire area. For rays, aerial surveys have been used to map
595 seagrass-meadow fragmentation caused by cownose ray foraging over a wide area of the shallow
596 subtidal bottom (Hovel and Lipcius, 2001; Orth, 1975). The present study has also made the
597 elevation contours of the target area in fine resolution, which is relevant to the understanding of
598 spatially varying utilization of tidal flats by high-tide predators incurring the risk of being stranded
599 with receding tides.
600 Ghost shrimp (Callianassidae) are one of the preferred food items for rays occurring in intertidal

601 (Harada and Tamaki, 2004; Howard et al., 1977; Tillett et al., 2008) and shallow subtidal (Ajemian
602 and Powers, 2013; Ebert and Cowley, 2003; Gray et al., 1997) sandy beds from wide geographic
603 regions. Furthermore, in intertidal sandflats, ghost shrimp burrows and ray feeding pits co-occur
604 sometimes both in high densities (D'Andrea et al., 2004; Martinell et al., 2001; Myrick and Flessa,
605 1996; Takeuchi et al., 2013). The larger stingrays can excavate the sediment deeper to obtain the
606 larger ghost shrimps residing in the lower portion of the sand column (Ebert and Cowley, 2003;
607 Tillett et al., 2008). Since ghost shrimps are powerful bioturbators themselves (Flach and Tamaki,
608 2001; Pillay and Branch, 2011), the ray–ghost shrimp relationship highlights a complex bioturbation
609 system in those sandflats. On the Tomioka sandflat, positive responses by stingrays to ghost shrimp
610 densities were found for the smallest fish-size groups, with the strong one in G1 and weak ones in
611 G2 and G3 (Figs. 7 and 8). There, feeding pit numbers gradually increased with shrimp numbers,
612 with no threshold prey density. As demonstrated for rays detecting the presence of infaunal buried
613 prey (Blonder and Alevizon, 1988; Montgomery and Skipworth, 1997; Tillett et al., 2008; Tilley et
614 al., 2013), stingrays may sense ghost shrimps by means of olfaction, electroreception, and
615 mechanoreception of water flow through shrimp burrow openings. If so, ghost-shrimp burrow
616 opening densities would serve as a cue for stingrays to excavate the sediment. The mean maximum
617 depths for the present six stingray feeding-pit groups, G1 to G6, were 6.5, 8.4, 10.7, 13.9, 17.8, and
618 22.3 cm, respectively (estimated from Figs. 4A and 5A). As the mean depth of the upper portion of
619 the adult *N. harmandi* burrow (above the node of the Y) is 9.6 cm (Tamaki and Ueno, 1998), the
620 excavation of sediment for ghost shrimps residing below the node in their burrows would be less
621 efficient for stingrays in G1 and G2 than in G3 to G6. Thus, by foraging in the area with higher prey
622 densities, the smallest stingrays could compensate for their inefficient gain per feeding bout.
623 Because of their individual smaller impact on ghost shrimps and medium population density (Fig.
624 5A), the smallest stingrays' prey-density-dependent foraging behavior would not have a significant

625 effect on the leveling off shrimp densities over the sandflat.

626 High-tide predators on tidal flats must withdraw to deeper waters during ebb tide. For the
627 Atlantic stingray, *Dasyatis americana*, spatial segregation was found within a shallow reef
628 environment, with beaches utilized by the smallest rays, deeper waters (> 10 m) by the largest ones,
629 and both by intermediate-sized ones (Aguiar et al., 2009). On the Tomioka sandflat, the larger
630 stingrays (G4–G6) foraged mainly in the lower shore (Figs. 6–9), suggesting that they are especially
631 cautious about the water-depth-range threshold to position themselves in (≥ 2.6 m at the highest tide).
632 The surface elevation higher by 0.5 m (Fig. 3A) was avoided by the larger stingrays. Thus ghost
633 shrimps in the upper shore escaped from the larger stingrays' predation (high-intertidal refuge). For a
634 dense population of the ghost shrimp, *Nihonotrypaea japonica*, inhabiting the upper part of an
635 extensive intertidal sandflat in Ariake Sound (Shirakawa sandflat), its recent severe decline, almost
636 to the extermination, is suspected to have been caused by increased predation pressure from *D.*
637 *akajei* (Takeuchi et al., 2013). In this case, large stingrays invaded as far as the uppermost shoreline
638 bounded by the concrete wall. Using the shore-normal elevation profiles (fig. 1C in Takeuchi et al.,
639 2013) and the temporal change in water level recorded at one point (Yamada et al., 2009) of the
640 sandflat, the highest water depth at the uppermost shore is estimated at 2.54 m. On the lower
641 Tomioka sandflat, ghost shrimps appeared to escape from predation to some extent around the
642 lowermost shoreline (Area VII: Fig. 3B) probably due to the thickest sand columns there (sediment
643 depth refuge), while they were subjected to the strongest predation pressure by the larger stingrays in
644 the more landward part from Area VII (i.e. Area IV) with the thinnest sand columns (Figs. 3E–H, 9,
645 and 10C–F). Although adult ghost shrimps were ingested by the larger stingrays, newly-recruited
646 juveniles appeared to be neglected (A. Tamaki, unpublished data), possibly having brought about an
647 alternate yearly change in shrimp density in Area IV (Fig. 3F–H). The sand-column thickness of the
648 *N. japonica*-inhabited zone of the Shirakawa sandflat (1–2 m; Wardiatno et al., 2003) is much

649 greater than that of the Tomioka sandflat (Fig. 3E), which might afford a sufficient sediment depth
650 refuge at the shrimp burrow bottom (70 cm below the surface; Tamaki and Ueno, 1998). However,
651 underground pore-water oxygen concentrations were more hypoxic on the Shirakawa sandflat (mean
652 concentrations 30 cm below the exposed sandflat surface, 3.8 mg l^{-1} in Tomioka versus 0.6 mg l^{-1} in
653 Shirakawa; Wardiatno et al., 2003). As the burrow of *N. japonica* has only a single surface opening,
654 with more limited water exchange with the overlying water column (Tamaki and Ueno, 1998), the
655 shrimp would come up nearer to the surface for ventilation.

656 Behavioral thermoregulation may explain the ontogenetic shift in the utilization of shallow
657 habitats by some ray species (Matern et al., 2000; Vaudo and Heithaus, 2013). This is unlikely to
658 occur in stingrays on the Tomioka sandflat, as swift flood currents over short intertidal distances
659 with a small elevation difference would rapidly mix the entire water mass (Sections 2.1 and 3.1).

660 Spatially varying foraging behaviors of rays within an intertidal habitat can generate
661 spatially-structured disturbance on the substrata (Hines et al., 1997). The estimation for the total area
662 disturbed by predators is confronted with a problem as to how the “total area” under study is
663 delimited, in which predators’ behavioral information can be used to define their feeding grounds
664 (Hall et al., 1994). On the Tomioka sandflat, the relatively low degrees of sediment excavation by
665 the smallest-size group of stingrays (G1: low individual bioturbation rate × medium abundance) and
666 the largest-size groups (G4–G6: high individual bioturbation rate × low abundance) were spatially
667 structured, owing to their respective utilization patterns for micro-habitats (Fig. 11). This spatial
668 heterogeneity was homogenized by the dominant intermediate-size groups in the population (G2 and
669 G3: medium individual bioturbation rate × high abundance), which appeared to be generalists in
670 selecting prey patch and sandflat elevation, resulting in both excavated-area and
671 displaced-sediment-volume densities over the sandflat confined to the small ranges by a factor of
672 1.6–1.7 (i.e. Sub-areas 1–6 versus 7+8: Fig. 11E,F).

673 As a first necessary step toward the proper assessment of sediment excavation rates by rays, we
674 examined the numerical, excavated-area, and displaced-sediment-volume densities of newly-formed
675 pits on a daily basis as a basic set of bioturbation rates and compiled published data (Table 2). The
676 papers showing at least two rates are listed in the table, excluding those only with data on
677 excavated-area proportion [e.g. 0.7–1.0% d^{-1} (Sherman et al., 1983)]. The reworking rate calculated
678 as (displaced-sediment-volume density per day) / (substratum area), which gives a vertical (*z*-axis)
679 sediment deposition rate on the substratum surface (e.g. D'Andrea et al., 2004), was also not
680 included, since locally displaced sediment is never spread homogeneously over the area.
681 Furthermore, the sediment turnover time, on either areal or volumetric basis, was not included. For
682 one thing, ray populations never regularly excavate sediment of the area one by one in a
683 non-overlapping pattern, often reusing formerly disturbed patches (Cross and Curran, 2004; O'Shea
684 et al., 2012; Fig. 2D–G). For another, reworking of the displaced sediment is done subsequently
685 through complex physical and biological processes in which ghost shrimp bioturbation is partly
686 involved (D'Andrea et al., 2004; Myrick and Flessa, 1996). In most of the previous studies, the three
687 bioturbation rates are not explicitly described. We estimated their (grand) mean values based on
688 ray pits' diameter, area, depth, and volume, and numerical density given in some of the original texts,
689 tables, and figures, and on our assumptions regarding "new pit" category, pit shape, and time-scale
690 adjustment of rates to daily basis (Table 2; see Appendix 3 for the table footnote descriptions). The
691 present study has achieved the largest total census area (11 ha versus previous 50 m^2–2.7 ha), with
692 heterogeneities in prey abundance and topography. The bioturbation rates by the stingray population
693 on the Tomioka sandflat are positioned at relatively high levels.
694 The present study has demonstrated the effectiveness of a combined aerial and manual survey to
695 provide one reliable way for measuring and estimating ray bioturbation rates in intertidal
696 soft-sediment habitats on a landscape scale. The procedure is applicable to the assessment of

disturbance by any surface-sediment excavators, especially by megafaunal biodiffusors, on tidal flats if their pit dimensions are discernible from the air. The present estimates were obtained based on the stingray's population structure and ontogenetic change in its heterogeneous micro-habitat utilizations as inferred from foraging trace abundance patterns. The basic premise of the study that feeding-pit size scales with fish size remains to be validated by observing actual fish behaviors. Finally, it must be pointed out that even under favorable weather and sea conditions over an entire spring-tide period enabling consecutive aerial photography, this time frame still poses limitations to the full understanding of the spatiotemporal dynamics of a foraging trace assembalge in tidal flats.

Acknowledgements

The aerial surveys were conducted in accord with the aviation law in Japan and under the permission of the local town office (Reihoku-cho, Kumamoto). We appreciate technical advice from H. Takase for aerial photogrammetry, and S. Shibata and S. Araki for help in processing images on the computer display. We thank Y. Hongo, Y. Saitoh, T. Nakano, S. Sen-ju, N. Takahashi, and A. Tanabe for assistance with field work. Numerous constructive comments and corrections were provided by the two anonymous reviewers. W. Collins kindly corrected the English text. This research was supported by the Environment Research and Technology Development Fund (4D-1104) of the Ministry of the Environment to AT.

Appendix 1. Detailed aerial survey methods and mosaic imaging conducted in 2012

All work below was carried out by Kyushu airlines, Co. (Oita, Japan). Flights were conducted on consecutive calm summer days at a height of 225 m during daytime low tides with nearly the same

721 water levels on 17 and 18 August 2012, using a manned helicopter equipped with an aerial film
722 camera (Hiei SE IIα, Osaka Optical Industry, Co., Ltd.). The photo-scale was aimed at 1/1500. Three
723 straight-line transects were set, with an overlap proportion between adjacent 172.5-m × 172.5-m unit
724 photographs aimed at 60% (Fig. 1D). Taking into account the possibility of halation from thin
725 surface waters on the exposed sandflat including those in stingray foraging traces, an excess number
726 of photographs was taken. They selected 35/65 photographs in Day 1 and 31/68 ones in Day 2 for
727 later treatment, resulting in 52–85% overlap (mean ± SD = 72.0 ± 4.4%). Aerial-based photography
728 took approximately 30 minutes to complete the task during the predicted lowest-tide time on each
729 date (13:45 and 14:21).

730 To convert the developed film into a digital image, the former was scanned with a resolution of
731 2540 dpi, using a high-accuracy scanner for photogrammetry (DSW500, LH Systems, Inc.). The
732 influences of camera-lens radial distortion and film development-associated expansion–contraction
733 on the developed films were corrected for each unit image (internal orientation), using a stereometric
734 system software (Stereometric/pro, Siscam S.r.l., Inc.). This software was also used for the
735 subsequent, external (= relative and absolute) orientations. After image processing, the final ground
736 resolution was 1.8 cm per pixel in the image, which was sufficient to detect the smallest stingray
737 foraging traces on the sanflat (see Fig. 2F,G).

738 In the relative orientation, an optical model for any two adjacent unit images was made, in which
739 at least six common points (tie points) must be lying in a balanced configuration in their overlapped
740 part. To fulfill this requirement, in July, 2012, a total of 65 marker points were arranged in and
741 around the sandflat every ca. 69 m in parallel to aerial transects and ca. 50 m perpendicular to them
742 (Fig. 1D, red circle points). Each marker point can be identified as the center of a square board or
743 sheet with 20 or 50 cm in side, painted in a checked pattern with two colors. At each marker point on
744 the sandflat, a plywood board was secured to a square timber that stood up to 25 cm above the

745 sandflat surface (see Fig. 2D,E). On the hard substrata surrounding the sandflat, a sheet was attached
746 to each marker-point plot. As the datum locations for these marker points, three second geographic
747 datum points established by the Geospatial Information Authority of Japan were available in close
748 vicinity to the target area, from which one additional datum point was newly installed (Fig. 1D,
749 white star marks; one datum point is outside the figure). The Cartesian coordinates (*x*, *y*, *z*) of the 65
750 marker points were determined from the three datum points indicated in Fig. 1D, using an electronic
751 total station (SOKKIA SET3030R, Topcon, Co.) before and after the aerial survey within a
752 maximum of 5-hour exposure time on 17 August 2012. In the present study, the elevations were
753 expressed as the values above the mean sea level at a tide gauge station of the Japan Meteorological
754 Agency located 6 km south of Tomioka Bay (130°02′E, 32°28′N; Fig. 1B, red star mark); the datum
755 points' elevations are described as deviations from the mean sea level of Tokyo Bay. The
756 coordinate-value errors were assessed by the measurement from two of the datum points toward five
757 of the marker points (Fig. 1D, denoted by asterisked white stars and red circle points), with their
758 mean ± SD being 2.86 ± 0.71 cm in longitude, 0.72 ± 0.81 cm in latitude, and 1.74 ± 0.69 cm in
759 elevation. Sometimes in the laboratory procedure, to achieve a more complete configuration of the
760 tie points for any two adjacent unit images, conspicuous natural markers were used in addition to
761 actual markers.

762 In the absolute orientation, each optical model constructed by the relative orientation was related
763 to the ground coordinate system based on the above 65 marker points. For this procedure, at least
764 three of these marker points (control points) must be lying in the overlapped part of any two adjacent
765 unit images (hereafter termed overlapped-part image). The actual number of control points ranged
766 from 3 to 10, with mean ± SD of 6.9 ± 1.4.

767 To attain images that are ortho-projected on a horizontal plane, first, the elevation contours were
768 drawn at 20-cm height intervals over the sandflat by stereoscopy for every overlapped-part image,

769 using Stereometric/pro. Tracing points on any one same elevation that were clearly visible on the
770 display automatically generated the corresponding contour line. The steep-slope artificial
771 constructions were treated separately from the sandflat region. The subsequent procedures were
772 conducted using an ortho-image production system software (New Orthomap, Siscam S.r.l., Inc.).
773 Based on the elevation contours, a digital elevation model (DEM) expressed as a triangulated
774 irregular network was constructed for the sandflat (Fig. 3A). All unit images were placed on the
775 DEM. For their ortho-projection, geometric correction (either elongating or shortening of images)
776 was made to correct for potential errors associated with camera inclination and the ground
777 topographic variations. Finally, all ortho-projected unit images were combined into a single mosaic
778 image over the sandflat for each date.
779
780 **Appendix 2. Detailed aerial survey methods conducted in 2011**
781
782 The work was carried out by Kaiteki-Kukan, Co., Ltd. (Fukuoka, Japan) and E-System, Co., Ltd.
783 (Hiroshima, Japan), using an unmanned helicopter (72 cm in round-shape diameter and 1.6 kg in
784 weight) equipped with GPS (MK-GPS 1.1, HiSystems GmbH, Co., Ltd.) and digital camera with
785 autofocus function (EOS Kiss X4 with 5184 × 3456 pixels, Canon, Inc.). It took about 2 hours for
786 them to complete the task between 12:30 and 14:30 including the lowest-tide time around 14:20, in
787 which photographed zones were varied with time according to the receding tide. The helicopter
788 automatically flew at a height of 50 m along ten GPS-programmed courses which were roughly in
789 parallel to the three ones used for the 2012 survey. One continual flight was restricted to 16 minutes
790 due to battery capacity. The position of the helicopter was being monitored on a personal computer
791 display. The camera shutter was released with a remote controller for each predetermined position,
792 with overlaps of 30–70% between adjacent ca. 93-m × 62-m unit images of which total number was

200. Twenty-two 15-cm × 15-cm square boards had been installed over the sandflat as the marker points.

Appendix 3. Descriptions for footnotes a–j in Table 2

[a] ND: mean number of pits newly formed per unit seabed area and unit time. EAD: mean of the area excavated by all newly-formed pits per unit seabed area and unit time = mean area excavated by a newly-formed pit × ND. DSVD: mean of the sediment volume displaced by all newly-formed pits per unit seabed area and unit time = mean sediment volume displaced by a newly-formed pit × ND.

[b] Number of census occasions: 8, each with a 4–6 d set. ND is calculated as a grand mean value for (1/100) × solid-bar values given in reference, fig. 10A. EAD is calculated as a grand mean value for 100 × solid-bar values given in reference, fig. 10C. DSVD is calculated as a grand mean value for 1000 × solid-bar values given in reference, fig. 10D.

[c] Number of census dates: 3. ND is calculated as a (1/60) × mean for the three values ("new pits") given in reference, table 1. EAD is calculated as a mean for the three values (100 × "percent of the area covered by new pits") given in reference, table 1. DSVD is calculated based on the assumption of half an ellipsoid for pit shape, with EAD and mean newly-formed pit depth (given in reference, text, p. 262: 10 cm).

[d] ND is calculated from a cumulative pit-diameter-frequency distribution recorded in a 300-m^2 plot over 7 days (given in reference, fig. 4). EAD is calculated from the same figure based on the assumption of a circle for pit plane shape, with the median in each diameter class used.

[e] Census time: after each tide; bioturbation rates are converted into those per day by multiplying by 2 due to the semi-diurnal tidal region. Number of census times: 18. ND is assumed to be a 2 × (grand mean value for the 18-tide data); "new pit density" value m^{-2} $tide^{-1}$ given in reference, table 2. Mean

817 excavated area of a newly-formed pit: 848 cm^2 (pit ellipse's mean long and short axes given in
818 reference, text, p. 38). Mean displaced-sediment volume of a newly-formed pit is given as 7400 cm^3
819 by the refilling procedure (reference, text, p. 38).
820 [f] Mean new-pit diameter: 26.8 cm, estimated from pit-diameter frequency distribution given in
821 reference, fig. 3. Mean excavated area of a newly-formed pit: 565.7 cm^2, based on the assumption of
822 a circle for pit plane shape. Mean depth of a newly-formed pit: 7.5 cm, based on the half the range
823 value, 5–10 cm, given in reference, text, p. 285. Mean displaced-sediment volume of a
824 newly-formed pit: 2828.3 cm^3, based on the assumption of half an ellipsoid for pit shape. ND is
825 calculated as (census area) × (areal proportion occupied by newly-formed pits given in reference,
826 text, p. 290: 0.0084) / (mean excavated area of a newly-formed pit).
827 [g] Number of census years: 3. Duration for each year census: 7 days. Daily total census area each
828 year: 1500 m^2. Total number of detected pits: 108. The areal proportion of these feeding pits in the
829 1500-m^2 survey area: 2.42% (given in reference, text, p. 192). The mean individual pit volume:
830 10064 cm^3 (given in reference, text, p. 192).
831 [h] Number of census dates: 6. Numerical density of pits: mean sum-total number of pits formed in
832 unit census area during the preceding four dates (reference, fig. 4). ND is assumed to be a grand
833 mean value for the six-date data calculated as (numerical density of pits) / (4 × 707). Mean
834 excavated area and depth of a newly-formed pit: 5000 cm^2 and 15 cm (reference, text, p. 196). EAD
835 is assumed to be a grand mean value for the six-date data. Mean displaced-sediment volume of a
836 newly-formed pit is assumed to be the volume of half an ellipsoid with the above mean excavated
837 area and depth values, being 50000 cm^3. DSVD is assumed to be a grand mean value for the six-date
838 data. The mean values of ND, EAD, and DSVD for the feeding pits corresponding to the prey
839 densities < threshold value (to elicit the predator's non-linear response) are estimated at 0.0029 m^{-2}
840 d^{-1}, 14.3 cm^2 m^{-2} d^{-1}, and 143.5 cm^3 m^{-2} d^{-1}, respectively. Those values corresponding to the prey

densities ≥ threshold value are 0.0083 m^{-2} d^{-1}, 41.6 cm^2 m^{-2} d^{-1}, and 416.0 cm^3 m^{-2} d^{-1}, respectively.

[i] ND (21 pits per 762 m^2 [= (724 + 800) / 2)] and mean diameter (80 cm) and depth (12 cm) for newly-formed pits are given in reference, text, p. 247. Individual mean pit area and mean pit volume are calculated based on the assumption of a circle and half a sphere for pit shapes, respectively.

[j] Based on Fig. 11. For ND, only pits are included (i.e. sinuous furrows are excluded), but for EAD and DSVD, both pits and sinuous furrows are included. The grand mean value for each sub-area group inclusive is given.

References

Aguiar, A.A., Valentin, J.L., Rosa, R.S., 2009. Habitat use by *Dasyatis americana* in a south-western Atlantic oceanic island. J. Mar. Biol. Assoc. U. K. 89, 1147–1152.

Ajemian, M.J., Powers, S.P., 2013. Foraging effects of cownose rays (*Rhinoptera bonasus*) along barrier islands of the northern Gulf of Mexico. J. Exp. Mar. Biol. Ecol. 439, 119–128.

Ajemian, M.J., Powers, S.P., Murdoch, T.J.T., 2012. Estimating the potential impacts of large mesopredators on benthic resources: integrative assessment of spotted eagle ray foraging ecology in Bermuda. PLoS One 7, e40227.

Akaike, H., 1973. Information theory and an extension of the maximum likelihood principle, in: Petrov, B.N., Csáki, F. (Eds.), Second International Symposium on Information Theory. Akadémiai Kiadó, Budapest, pp. 267–281.

Beisiegel, B.M., Mantovani, W., 2006. Habitat use, home range and foraging preferences of the coati *Nasua nasua* in a pluvial tropical Atlantic forest area. J. Zool. 269, 77–87.

Blonder, B.I., Alevizon, W.S., 1988. Prey discrimination and electroreception in the stingray *Dasyatis sabina*. Copeia 1988, 33–36.

Botton, M.L., 1984. The importance of predation by horseshoe crabs, *Limulus polyphemus*, to an intertidal sand flat community. J. Mar. Res. 42, 139–161.

867 Bromley, R.G., 1996. Trace Fossils, second ed. Chapman and Hall, London.

868 Cadée, G.C., 1990. Feeding traces and bioturbation by birds on a tidal flat, Dutch Wadden Sea.
869 Ichnos 1, 23–30.

870 Cadée, G.C., 2001. Sediment dynamics by bioturbating organisms, in: Reise, K. (Ed.), Ecological
871 Comparisons of Sedimentary Shores. Springer, Berlin, pp. 127–148.

872 Calenge, C., 2006. The package "adehabitat" for the R software: a tool for the analysis of space and
873 habitat use by animals. Ecol. Model. 197, 516–519.

874 Cartamil, D.P., Vaudo, J.J., Lowe, C.G., Wetherbee, B.M., Holland, K.N., 2003. Diel movement
875 patterns of the Hawaiian stingray, *Dasyatis lata*: implications for ecological interactions
876 between sympatric elasmobranch species. Mar. Biol. 142, 841–847.

877 Cross, R.E., Curran, M.C., 2004. Recovery of meiofauna in intertidal feeding pits created by rays.
878 Southeast. Nat. 3, 219–230.

879 D'Andrea, A.F., Lopez, G.R., Aller, R.C., 2004. Rapid physical and biological particle mixing on an
880 intertidal sandflat. J. Mar. Res. 62, 67–92.

881 Ebert, D.A., Cowley, P.D., 2003. Diet, feeding behaviour and habitat utilisation of the blue stingray
882 *Dasyatis chrysonota* (Smith, 1828) in South African waters. Mar. Freshw. Res. 54, 957–965.

883 Flach, E., Tamaki, A., 2001. Competitive bioturbators on intertidal sand flats in the European
884 Wadden Sea and Ariake Sound in Japan, in: Reise, K. (Ed.), Ecological Comparisons of
885 Sedimentary Shores. Springer, Berlin, pp. 149–171.

886 Grant, J., 1983. The relative magnitude of biological and physical sediment reworking in an
887 intertidal community. J. Mar. Res. 41, 673–689.

888 Gray, A.E., Mulligan, T.J., Hannah, R.W., 1997. Food habits, occurrence, and population structure
889 of the bat ray, *Myliobatis californica*, in Humboldt Bay, California. Environ. Biol. Fishes 49,
890 227–238.

891 Gregory, M.R., Ballance, P.F., Gibson, G.W., Ayling, A.M., 1979. On how some rays
892 (Elasmobranchia) excavate feeding depressions by jetting water. J. Sediment. Petrol. 49, 1125–
893 1130.

894 Hall, S.J., Basford, D.J., Robertson, M.R., Raffaelli, D.G., Tuck, I., 1991. Patterns of recolonisation
895 and the importance of pit-digging by the crab *Cancer pagurus* in a subtidal sand habitat. Mar.
896 Ecol. Prog. Ser. 72, 93–102.

897 Hall, S.J., Raffaelli, D., Thrush, S.F., 1994. Patchiness and disturbance in shallow water benthic
898 assemblages, in: Giller, P.S., Hildrew, A.G., Raffaelli, D.G. (Eds.), Aquatic Ecology: Scale,
899 Pattern and Process. Blackwell Scientific Publications, Oxford, pp. 333–375.

900 Harada, K., Tamaki, A., 2004. Assessment of the predation impact of the stingray *Dsyatis akajei*
901 (Müller & Henle, 1841) on the population of the ghost shrimp *Nihonotrypaea harmandi*
902 (Bouvier, 1901) on an intertidal sandflat (preliminary report), in: Tamaki, A. (Ed.), Proceeding
903 of the Symposium on "Ecology of Large Bioturbators in Tidal Flats and Shallow Sublittoral
904 Sediments – from Individual Behavior to Their Role as Ecosystem Engineers". Nagasaki
905 University, Nagasaki, pp. 81–85.

906 Heithaus, M.R., Frid, A., Vaudo, J.J., Worm, B., Wirsing, A.J., 2010. Unraveling the ecological
907 importance of elasmobranchs, in: Carrier, J.C., Musick, J.A., Heithaus, M.R. (Eds.), Sharks
908 and Their Relatives II. CRC Press, Boca Raton, pp. 611–637.

909 Hines, A.H., Loughlin, T.R., 1980. Observations of sea otters digging for clams at Monterey Harbor,
910 California. Fish. Bull. 78, 159–163.

911 Hines, A.H., Whitlatch, R.B., Thrush, S.F., Hewitt, J.E., Cummings, V.J., Dayton, P.K., Legendre,
912 P., 1997. Nonlinear foraging response of a large marine predator to benthic prey: eagle ray pits
913 and bivalves in a New Zealand sandflat. J. Exp. Mar. Biol. Ecol. 216, 191–210.

914 Hovel, K.A., Lipcius, R.N., 2001. Habitat fragmentation in a seagrass landscape: patch size and
915 complexity control blue crab survival. Ecology 82, 1814–1829.

916 Howard, J.D., Mayou, T.V., Heard, R.W., 1977. Biogenic sedimentary structures formed by rays. J.
917 Sediment. Petrol. 47, 339–346.

918 Johnson, K.R., Nelson, C.H., 1984. Side-scan sonar assessment of gray whale feeding in the Bering
919 Sea. Science 225, 1150–1152.

920 Kristensen, E., Penha-Lopes, G., Delefosse, M., Valdemarsen, T., Quintana, C.O., Banta, G.T., 2012.
921 What is bioturbation? The need for a precise definition for fauna in aquatic sciences. Mar. Ecol.
922 Prog. Ser. 446, 285–302.

923 Lazar, B., Gračan, R., Katić, J., Zavodnik, D., Jaklin, A., Tvrtković, N., 2011. Loggerhead sea turtles
924 (*Caretta caretta*) as bioturbators in neritic habitats: an insight through the analysis of benthic
925 molluscs in the diet. Mar. Ecol. 32, 65–74.

926 Lee, W.-J., 2010. Intensive use of an intertidal mudflat by foraging adult American horseshoe crabs
927 *Limulus polyphemus* in the Great Bay estuary, New Hampshire. Curr. Zool. 56, 611–617.

928 Mandal, S., Tamaki, A., Ohashi, S., Takeuchi, S., Agata, Y., Takahara, Y., Harada, K., Yamada, F.,
929 2010. How newly recruited cohorts are formed in the trochid gastropod population (*Umbonium*
930 *moniliferum*) on an intertidal sandflat in western Kyushu, Japan. J. Exp. Mar. Biol. Ecol. 389,
931 18–37.

932 Martinell, J., De Gibert, J.M., Domènech, R., Ekdale, A.A., Steen, P.P., 2001. Cretaceous ray
933 traces?: an alternative interpretation for the alleged dinosaur tracks of La Posa, Isona, NE
934 Spain. Palaios 16, 409–416.

935 Matern, S.A., Cech, J.J.,Jr., Hopkins, T.E., 2000. Diel movements of bat rays, *Myliobatis californica*,
936 in Tomales Bay, California: evidence for behavioral thermoregulation? Environ. Biol. Fish., 58,
937 173–182.

938 Meysman, F.J.R., Middelburg, J.J., Heip, C.H.R., 2006. Bioturbation: a fresh look at Darwin's last
939 idea. Trends Ecol. Evol. 21, 688–695.

940 Montgomery, J., Skipworth, E., 1997. Detection of weak water jets by the short-tailed stingray
941 *Dasyatis brevicaudata* (Pisces: Dasyatidae). Copeia 1997, 881–883.

942 Myers, R.A., Baum, J.K., Shepherd, T.D., Powers, S.P., Peterson, C.H., 2007. Cascading effects of
943 the loss of apex predatory sharks from a coastal ocean. Science 315, 1846–1850.

944 Myrick, J.L., Flessa, K.W., 1996. Bioturbation rates in Bahía La Choya, Sonora, Mexico. Ciencias
945 Mar. 22, 23–46.

946 Nacken, M., Reise, K., 2000. Effects of herbivorous birds on intertidal seagrass beds in the northern
947 Wadden Sea. Helgol. Mar. Res. 54, 87–94.

948 Nelson, C.H., Johnson, K.R., Barber, J.H., Jr., 1987. Gray whale and walrus feeding excavation on
949 the Bering Shelf, Alaska. J. Sediment. Petrol. 57, 419–430.

950 O'Shea, O.R., Thums, M., van Keulen, M., Meekan, M., 2012. Bioturbation by stingrays at Ningaloo
951 Reef, Western Australia. Mar. Freshw. Res. 63, 189–197.

952 Oliver, J.S., Kvitek, R.G., Slattery, P.N., 1985. Walrus feeding disturbance: scavenging habits and
953 recolonization of the Bering Sea benthos. J. Exp. Mar. Biol. Ecol. 91, 233–246.

954 Orth, R.J., 1975. Destruction of eelgrass, *Zostera marina*, by the cownose ray, *Rhinoptera bonasus*,
955 in the Chesapeake Bay. Chesap. Sci. 16, 205–208.

956 Pebesma, E.J., 2004. Multivariable geostatistics in S: the gstat package. Comput. Geosci. 30, 683–
957 691.

958 Peterson, C.H., Fodrie, F.J., Summerson, H.C., Powers, S.P., 2001. Site-specific and
959 density-dependent extinction of prey by schooling rays: generation of a population sink in
960 top-quality habitat for bay scallops. Oecologia 129, 349–356.

961 Pillay, D., Branch, G.M., 2011. Bioengineering effects of burrowing thalassinidean shrimps on
962 marine soft-bottom ecosystems. Oceanogr. Mar. Biol. Annu. Rev. 49, 137–192.

963 Preen, A., 1995. Impacts of dugong foraging on seagrass habitats: observational and experimental
964 evidence for cultivation grazing. Mar. Ecol. Prog. Ser. 124, 201–213.

965 Quantum GIS Development Team, 2012. Quantum GIS geographic information system.

966 R Core Team, 2012. R: a language and environment for statistical computing.

967 Ray, G.C., McCormick-Ray, J., Berg, P., Epstein, H.E., 2006. Pacific walrus: benthic bioturbator of
968 Beringia. J. Exp. Mar. Biol. Ecol. 330, 403–419.

969 Reidenauer, J.A., Thistle, D., 1981. Response of a soft-bottom harpacticoid community to stingray
970 (*Dasyatis sabina*) disturbance. Mar. Biol. 65, 261–267.

971 Ribeiro, P.J., Jr., Diggle, P.J., 2001. geoR: a package for geostatistical analysis. R-News 1, 15–18.

972 Sasko, D.E., Dean, M.N., Motta, P.J., Hueter, R.E., 2006. Prey capture behavior and kinematics of
973 the Atlantic cownose ray, *Rhinoptera bonasus*. Zoology 109, 171–181.

974 Sherman, K.M., Reidenauer, J.A., Thistle, D., Meeter, D., 1983. Role of a natural disturbance in an
975 assemblage of marine free-living nematodes. Mar. Ecol. Prog. Ser. 11, 23–30.

976 Skilleter, G.A., Wegscheidl, C., Lanyon, J.M., 2007. Effects of grazing by a marine mega-herbivore
977 on benthic assemblages in a subtropical seagrass bed. Mar. Ecol. Prog. Ser. 351, 287–300.

978 Takeuchi, S., Takahara, Y., Agata, Y., Nasuda, J., Yamada, F., Tamaki, A., 2013. Response of
979 suspension-feeding clams to natural removal of bioturbating shrimp on a large estuarine
980 intertidal sandflat in western Kyushu, Japan. J. Exp. Mar. Biol. Ecol. 448, 308–320.

981 Tamaki, A., 1984. Structural characteristics of an intertidal sand flat in Tomioka Bay, Amakusa,
982 west Kyushu. Publ. Amakusa Mar. Biol. Lab. Kyushu Univ. 7, 125–150.

983 Tamaki, A., 1987. Comparison of resistivity to transport by wave action in several polychaete
984 species on an intertidal sand flat. Mar. Ecol. Prog. Ser. 37, 181–189.

985 Tamaki, A., Ingole, B., 1993. Distribution of juvenile and adult ghost shrimps, *Callianassa japonica*
986 Ortmann (Thalassinidea), on an intertidal sand flat: intraspecific facilitation as a possible
987 pattern-generating factor. J. Crustac. Biol. 13, 175–183.

988 Tamaki, A., Ingole, B., Ikebe, K., Muramatsu, K., Taka, M., Tanaka, M., 1997. Life history of the
989 ghost shrimp, *Callianassa japonica* Ortmann (Decapoda: Thalassinidea), on an intertidal
990 sandflat in western Kyushu, Japan. J. Exp. Mar. Biol. Ecol. 210, 223–250.

991 Tamaki, A., Ueno, H., 1998. Burrow morphology of two callianassid shrimps, *Callianassa japonica*
992 Ortmann, 1891 and *Callianassa* sp. (= *C. japonica*: de Man, 1928) (Decapoda: Thalassinidea).
993 Crustac. Res. 27, 28–39.

994 Taniuchi, T., Shimizu, M., 1993. Dental sexual dimorphism and food habits in the stingray *Dasyatis*
995 *akajei* from Tokyo Bay, Japan. Nippon Suisan Gakkaishi 59, 53–60.

996 Thrush, S.F., 1986. Spatial heterogeneity in subtidal gravel generated by the pit-digging activities of
997 *Cancer pagurus*. Mar. Ecol. Prog. Ser. 30, 221–227.

998 Thrush, S.F., Pridmore, R.D., Hewitt, J.E., Cummings, V.J., 1991. Impact of ray feeding
999 disturbances on sandflat macrobenthos: do communities dominated by polychaetes or shellfish
1000 respond differently? Mar. Ecol. Prog. Ser. 69, 245–252.

1001 Tillett, B.J., Tibbetts, I.R., Whithead, D.L., 2008. Foraging behaviour and prey discrimination in the
1002 bluespotted maskray *Dasyatis kuhlii*. J. Fish Biol. 73, 1554–1561.

1003 Tilley, A., López-Angarita, J., Turner, J.R., 2013. Effects of scale and habitat distribution on the
1004 movement of the southern stingray *Dasyatis americana* on a Caribbean atoll. Mar. Ecol. Prog.
1005 Ser. 482, 169–179.

1006 Valentine, J.F., Heck, K.L., Jr., Harper, P., Beck, M., 1994. Effects of bioturbation in controlling
1007 turtlegrass (*Thalassia testudinum* Banks *ex* König) abundance: evidence from field enclosures
1008 and observations in the Northern Gulf of Mexico. J. Exp. Mar. Biol. Ecol. 178, 181–192.

1009 VanBlaricom, G.R., 1982. Experimental analyses of structural regulation in a marine sand
1010 community exposed to oceanic swell. Ecol. Monogr. 52, 283–305.

1011 Vaudo, J.J., Heithaus, M.R., 2013. Microhabitat selection by marine mesoconsumers in a thermally
1012 heterogeneous habitat: behavioral thermoregulation or avoiding predation risk? PLoS One 8,
1013 e61907.

1014 Villegas-Ríos, D., Alós, J., March, D., Palmer, M., Mucientes, G., Saborido-Rey, F., 2013. Home
1015 range and diel behavior of the ballan wrasse, *Labrus bergylta*, determined by acoustic
1016 telemetry. J. Sea Res. 80, 61–71.

1017 Wardiatno, Y., Shimoda, K., Koyama, K., Tamaki, A., 2003. Zonation of congeneric callianassid
1018 shrimps, *Nihonotrypaea harmandi* (Bouvier, 1901) and *N. japonica* (Ortmann, 1891)
1019 (Decapoda: Thalassinidea), on intertidal sandflats in the Ariake-Sound estuarine system,
1020 Kyushu, Japan. Benthos Res. 58, 51–73.

1021 Weitkamp, L.A., Wissmar, R.C., Simenstad, C.A., Fresh, K.L., Odell, J.G., 1992. Gray whale
1022 foraging on ghost shrimp (*Callianassa californiensis*) in littoral sand flats of Puget Sound,
1023 U.S.A. Can. J. Zool. 70, 2275–2280.

1024 Woodin, S.A., 1978. Refuges, disturbance, and community structure: a marine soft-bottom example.
1025 Ecology 59, 274–284.

1026 Worton, B.J., 1989. Kernel methods for estimating the utilization distribution in home-range studies.
1027 Ecology 70, 164–168.

1028 Yahel, G., Yahel, R., Katz, T., Lazar, B., Herut, B., Tunnicliffe, V., 2008. Fish activity: a major
1029 mechanism for sediment resuspension and organic matter remineralization in coastal marine
1030 sediments. Mar. Ecol. Prog. Ser. 372, 195–209.

1031 Yahel, R., Yahel, G., Genin, A., 2002. Daily cycles of suspended sand at coral reefs: a biological
1032 control. Limnol. Oceanogr. 47, 1071–1083.

1033 Yamada, F., Kobayashi, N., Sakanishi, Y., Tamaki, A., 2009. Phase averaged suspended sediment
1034 fluxes on intertidal mudflat adjacent to river mouth. J. Coast. Res. 25, 350–358.

1035 Yamaguchi, A., 2005. On the yearly catch variation of rays in Ariake Sound. Rep. Jpn. Soc. for
1036 Elasmobranch Stud. 41, 8–12. (in Japanese).

1037

1038

1039

1040

1041

1042

1043

1044

1045

1046

1047

1048

1049

1050

1051

1052

1053

1054

1055

Figure captions

Fig. 1. Study site. **A–D**: Intertidal sandflat facing Tomioka Bay (Tomioka sandflat) on the northwestern corner of Amakusa-Shimoshima Island in western Kyushu, Japan. **B**, red star: tide gauge station of the Japan Meteorological Agency located 6 km south of Tomioka Bay. **D**, white-colored area: aerial survey domain in 2012 (107516 m^2 in exposed area). That survey domain in 2011 was extended 20–60 m seaward to the level of the mean low water at spring tides (blue line). Stingray foraging traces were invisible in a narrow strip covered with green algae (*Ulva pertusa*) along the uppermost shoreline. The cross mark: point installed with water-pressure gauge. The red filled circles: marker points for the 2012 aerial survey. The white stars: datum points for determining the coordinates of these marker points. The asterisked circles and stars: points used for assessing coordinate-value errors. The flight in 2012 was conducted along the three dotted lines, with a unit photographed areal coverage exemplified as the red dotted square.

Fig. 2. Stingray foraging traces. Foraging trace images on the exposed Tomioka sandflat in 2012, taken on the ground (**A,B**) and from the air (**C–G**). **A,B**: Fragments of green algae trapped in some traces. Black spots seen on the sandflat surface are openings of ghost shrimp burrows. **C**: Close-up view of feeding pits (FP) and sinuous furrows (SF). **D,E** and **F,G**: Identical plots taken on 17 and 18 August, respectively. One 20-cm × 20-cm marker point is indicated by the arrows in **D** and **E**. The darker parts stand for foraging traces of varying ages, with the newly-formed feeding pits and sinuous furrows indicated red and blue, respectively, in **E** and **G**. The two feeding pits with black and red arrows in each of **F** and **G** indicate their degradation with infilled sediment in one day.

Fig. 3. Sandflat feature and ghost shrimp distribution maps. Environmental characteristics (**A–E**)

and ghost shrimp density (**F–H**) over the Tomioka sandflat. In all panels, the outline of the 2012 aerial survey domain is indicated (Fig. 1D). **A**: Elevation profile by the ordinary Kriging interpolation based on 2-m mesh Digital Elevation Model (DEM), with values given as heights from the mean sea level at the tide gauge station (Fig. 1B). **B**: Division of the sandflat into sub-areas with regard to a boundary elevation of 0.56 m (**A**) and position; Area VII was exposed only in the 2011 aerial survey. **C**,**D**: Estimated isopleths of submergence duration in the first and second tides during 17 to 18 August 2012, based on the water-level record at the cross-marked point (Fig. 1D) and elevation profile (**A**). **E**: Sand-column thickness distribution by the ordinary Kriging interpolation based on measurements at dot points. **F**,**G**,**H**: *Nihonotrypaea harmandi* numerical density distributions by the ordinary Kriging interpolation based on burrow-opening counts at dot points in 2011, 2012, and 2013, respectively.

Fig. 4. Scatter plots for relationships among three dimensions of stingray foraging traces on the Tomioka sandflat. **A**: Maximum-depth (cm) and area (m^2) for newly-formed feeding pits, with the solid regression curve [$Depth = 0.6 \times (10^4 Area)^{0.4}$] from the 2012 survey and with the upper and lower broken regression curves from a previous survey result (A. Tamaki, unpublished data; equations given in Section 2.5, text; *N*, number of pits); the appropriateness of judgment for the "newly formed" in 2012 was confirmed by the maximum-depth ranges for the newly-formed pits as identified from the manual survey over two consecutive dates in the previous survey. **B**: Depth (cm) and area (m^2) for sinuous furrows associated with newly-formed feeding pits, with 1–19 measurement plots varying with individual furrow sizes (different symbols for furrow identities) and the grand mean depth of 4.2 cm (dotted line). **C**: Infilled sediment volume (cm^3) and area (m^2) for the feeding pits (**A**), with the regression curve given as $Volume = 50011.3 / (1 + 28.4 \exp(-8.5 Area))$. **D**: Infilled sediment volume (cm^3) and area (m^2) for the sinuous furrows (**B**), with the regression

curve given as $Volume = 34.2 \times (10^4 Area)^{0.7}$.

Fig. 5. Stingray foraging trace areal frequency distributions and scatter plots. **A–C**: Area-frequency distributions of newly-formed foraging traces over the Tomioka sandflat (*N*: number of traces), as obtained from the 2012 aerial survey. **A**: Feeding pits, with a unit-area class of 0.05 m^2 and the subdivision into six groups (G1–G6; see text for their boundary values and number of pits for each group). **B**: All sinuous furrows, with a unit area-class of 0.2 m^2. **C**: Feeding pits accompanied by sinuous furrows, with those ≥ 0.25 m^2 in area demarcated for analysis of data in Fig. 9. **D**: Relationship between feeding-pit-associated sinuous-furrow area and feeding-pit area, with respective paired data extracted from **B** and **C**.

Fig. 6. Distribution of newly-formed stingray foraging traces by size. **A**: feeding pits. **B**: sinuous furrows. *N*: number of traces detected in the 2012 aerial survey domain on the Tomioka sandflat. Each trace is placed at the (*x*, *y*)-coordinate of its center position and expressed by a semi-transparent circle in proportion to each area.

Fig. 7. Kernel home ranges (95% and 50%) of newly-formed stingray feeding pits by their size groups. **A**–**F**: G1–G6 (defined in Fig. 5A) in the 2012 aerial survey domain of the Tomioka sandflat.

Fig. 8. Generalized linear model (GLM) fitting. Graphic representations of the result of fitting to test for the selectivity of stingrays of respective size groups [G1–G6 (Fig. 5A) arranged in columns] for prey (ghost shrimp) density and/or topographic elevation on the Tomioka sandflat. See Table 1 for parameter values in the best fit. The explanatory variables used are given in the four models arranged in rows: prey density alone (Model 1), sandflat elevation alone (Model 2), and both prey

density and elevation (Model 3); Model 4 (null model: indifferent to both prey density and elevation) was never adopted in all G*n*s and are not shown. The percentage values in the three panels for each of G*n*s indicate their adoption rates as best fit in each 99 runs. The best-fit case based on AIC is displayed for each model.

Fig. 9. Distribution of the larger stingray feeding pits. **A**: For those pits newly-formed with ≥ 0.25 m^2 in area (Fig. 5C: G4–G6) over the 2012 aerial survey domain of the Tomioka sandflat. The density classes divided by Natural Breaks (Jenks) mode are assigned to each 10-m × 10-m unit grid cell. **B**: For those pits of all ages inclusive at 55 randomly-generated 20-m diameter circles (center positions indicated by cross marks) over the 2011 aerial survey domain, with Areas IV and VII (Fig. 3B) highlighted. For comparison with the densities in 2012, the number of pits contained in each census circle was converted into the value per 100 m^2 and expressed by a gray circle area.

Fig. 10. Distribution of stingray bioturbation rates and depth over the Tomioka sandflat. **A**: Distribution of the excavated-area density of all newly-formed stingray foraging traces inclusive for each 10-m × 10-m grid cell over the 2012 aerial survey domain of the sandflat. The densities of traces were divided into classes by Quantile mode. **B**: Distribution of the displaced-sediment-volume density of these traces over the sandflat, as estimated based on each trace's area (Fig. 6A,B) and the regression equation of volume versus area for the traces obtained by the *in situ* survey (Fig. 4C,D). The densities of traces were divided into classes as in **A**. **C**–**F**: Distribution of the percentage proportion of maximum depth (PPMD) of each newly-formed feeding pit in the sand column of the corresponding point over the sandflat; the PPMDs are divided into four classes. Each value is expressed by a semi-transparent gray circle area. The maximum depth for each pit was estimated based on its area (Fig. 6A) and the regression equation of maximum depth versus area for the pits

obtained by the *in situ* survey (Fig. 4A). The target area of the sandflat was limited to that for the sand-column thickness survey (Fig. 3E).

Fig. 11. Division of the Tomioka sandflat by stingray bioturbation rates. **A**: Division into eight sub-areas based on elevation and ghost shrimp density at each 10-m × 10-m grid cell. The whole area was determined according to the overlapped part among the aerial, elevation, and ghost-shrimp density surveys conducted in 2012 (Figs. 1D, 3A,G). White parts: no complete data set available. See text for the boundary values for the low, mid/medium, and high categories in elevation and ghost shrimp density. **B**: Sum total area for each sub-area. **C**: Sum total of the excavated areas of stingray foraging traces for each sub-area, with contributions of respective foraging-trace groups stacked (G1–G6, feeding pits and SF, sinuous furrow). **D**: Sum total of the estimated displaced-sediment volumes of foraging traces for each sub-area. **E**: Excavated-area density of foraging traces for each sub-area. **F**: Estimated displaced-sediment-volume density of foraging traces for each sub-area.

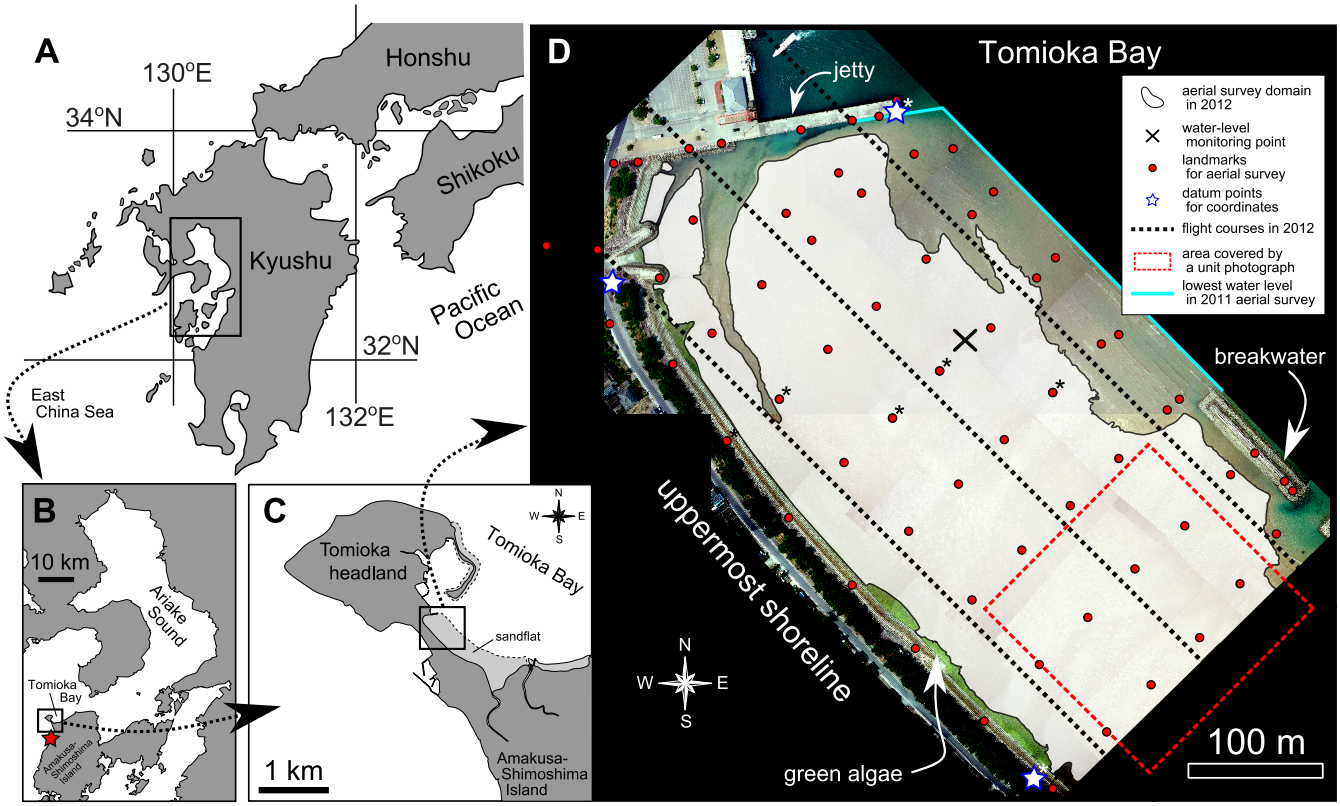

Fig. 1 (Takeuchi and Tamaki, revised)

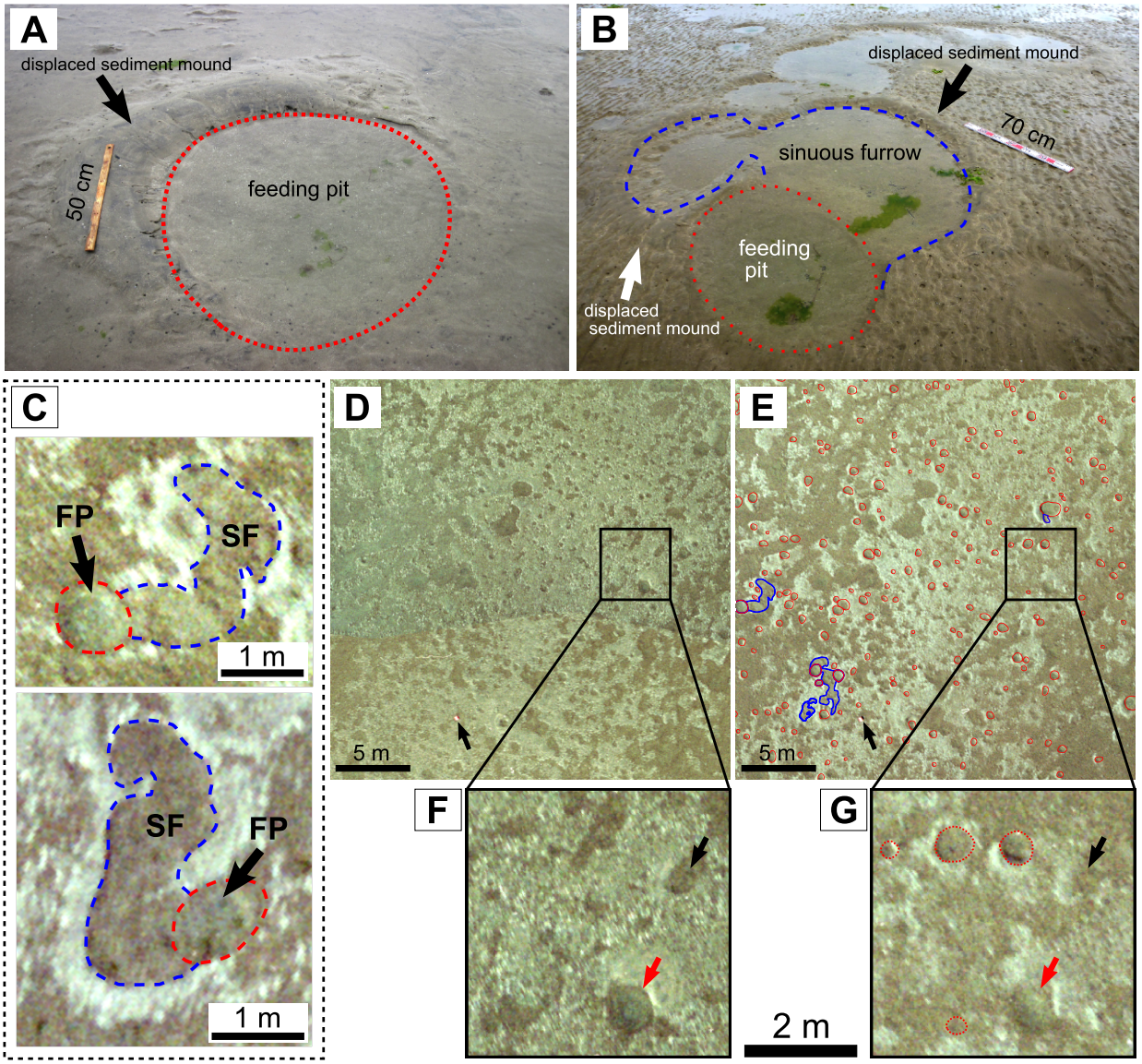

Fig. 2 (Takeuchi and Tamaki, revised)

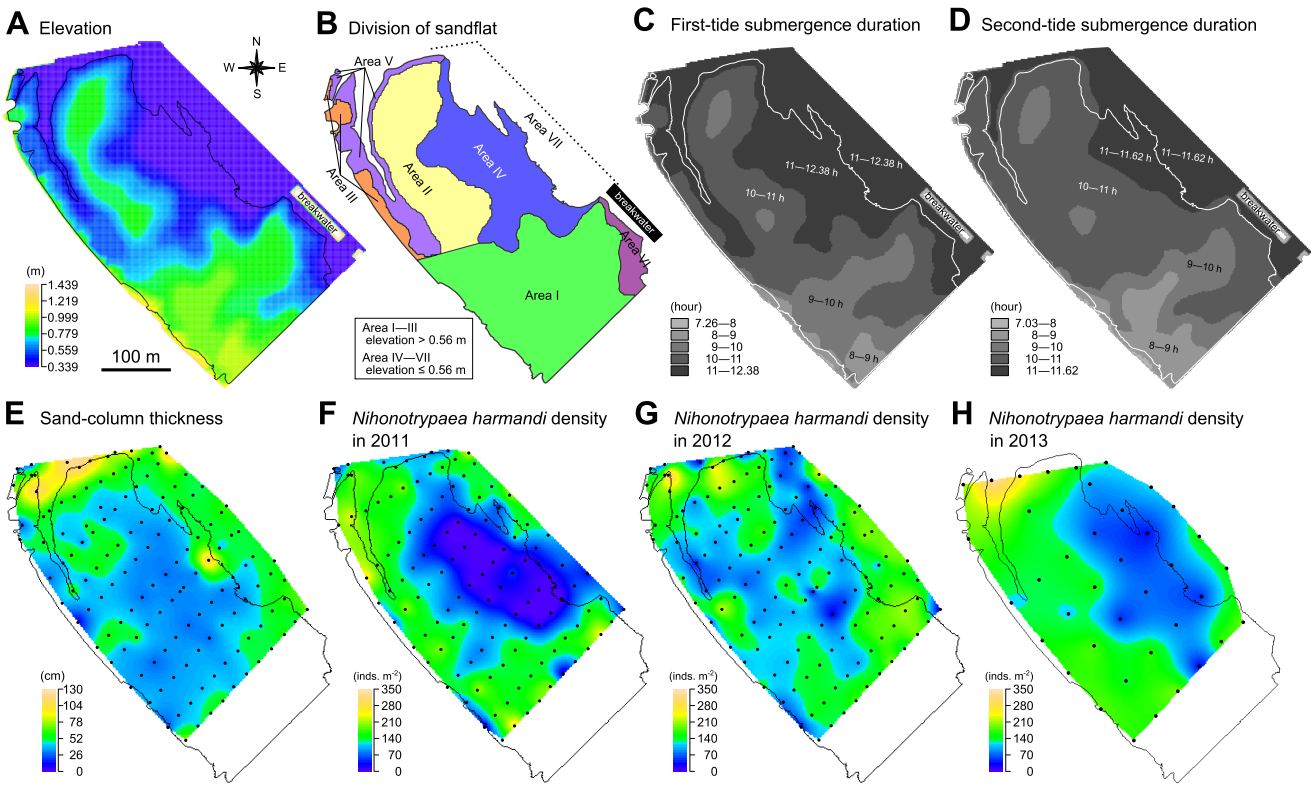

Fig. 3 (Takeuchi and Tamaki, revised)

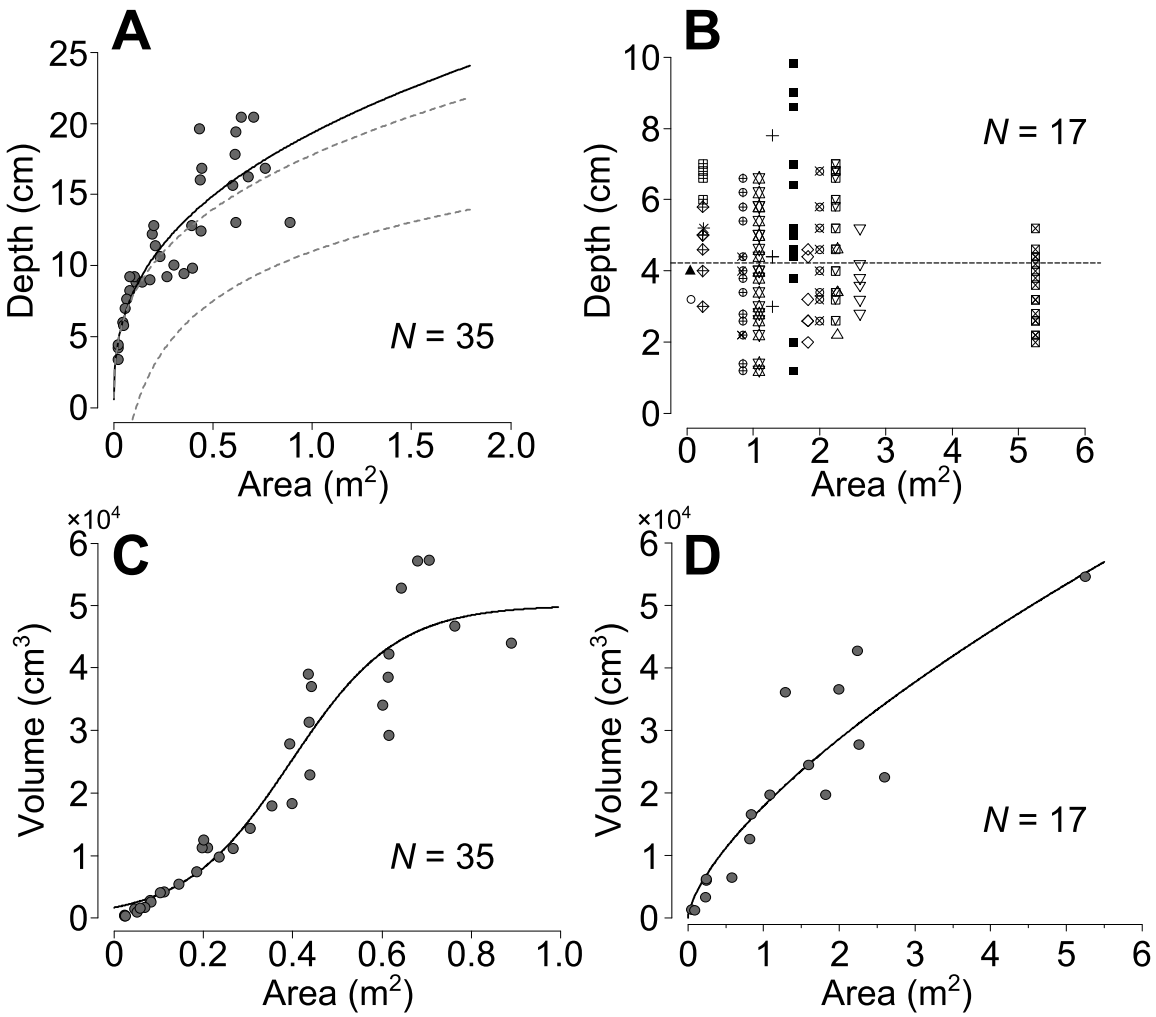

Fig. 4 (Takeuchi and Tamaki, revised)

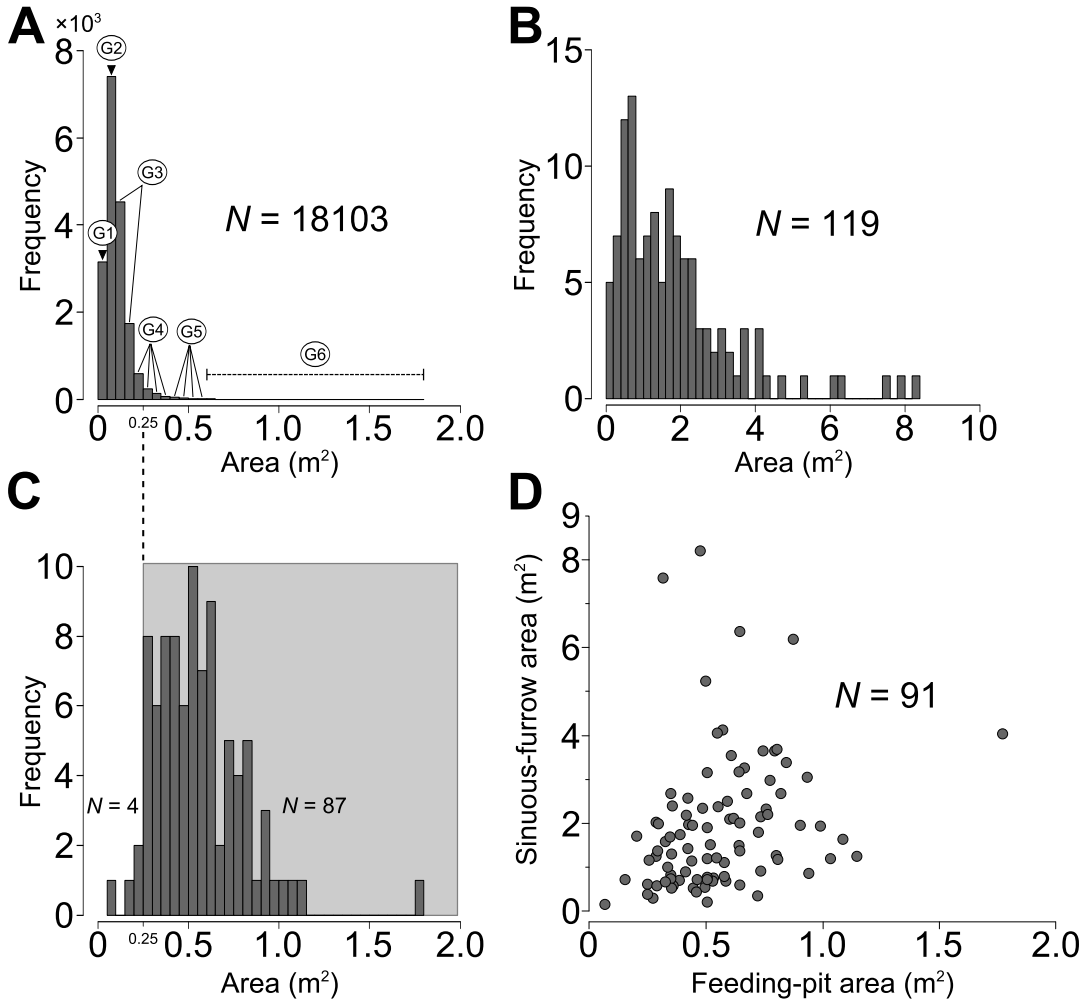

Fig. 5 (Takeuchi and Tamaki, revised)

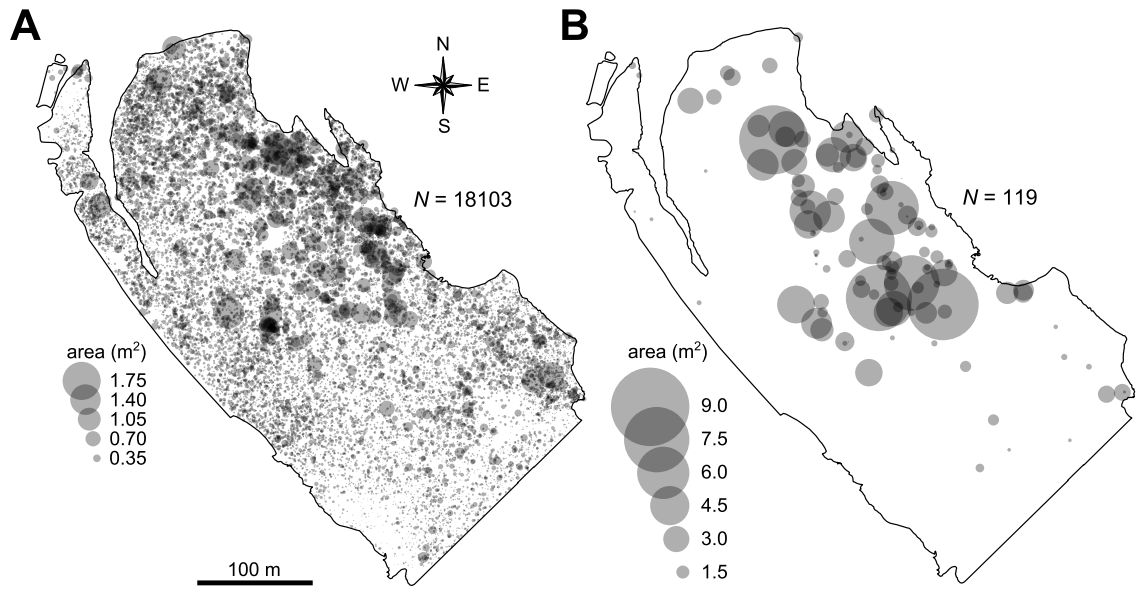

Fig. 6 (Takeuchi and Tamaki, revised)

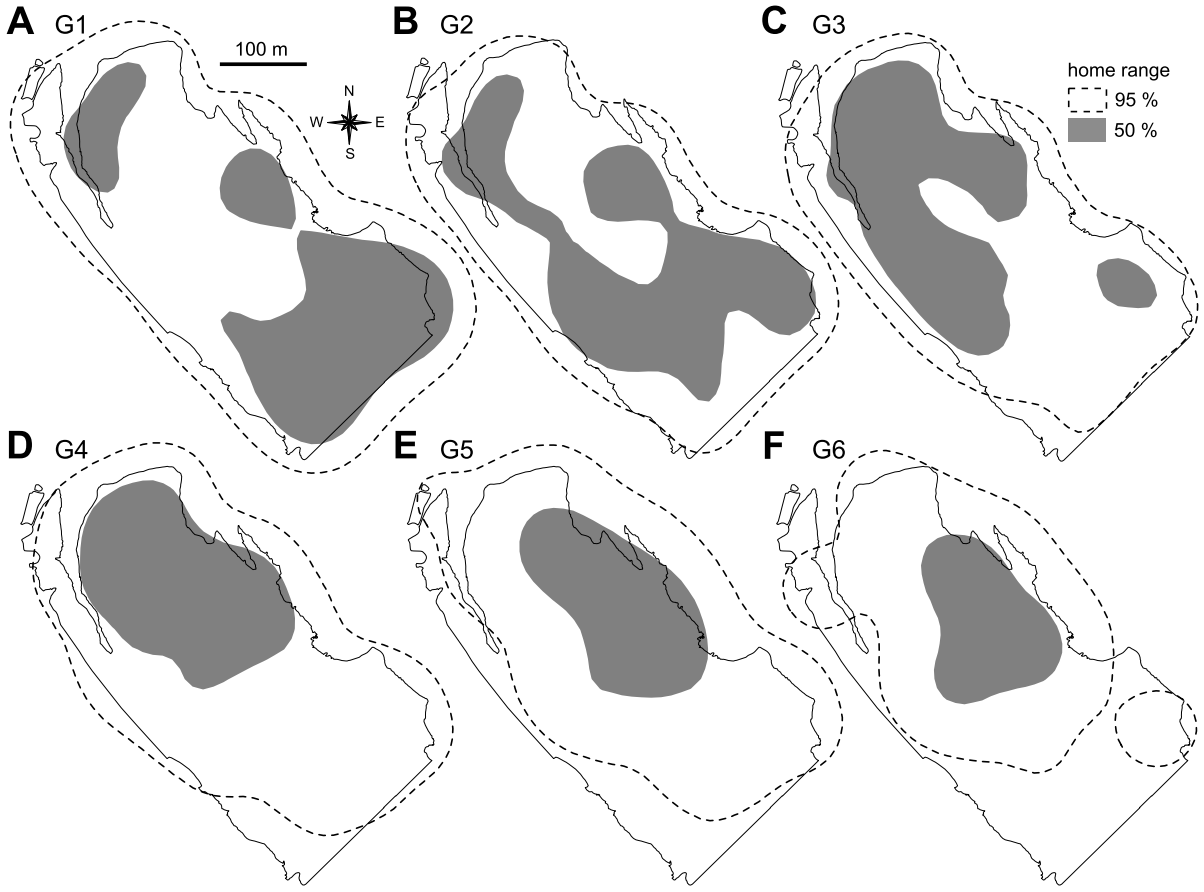

Fig. 7 (Takeuchi and Tamaki, revised)

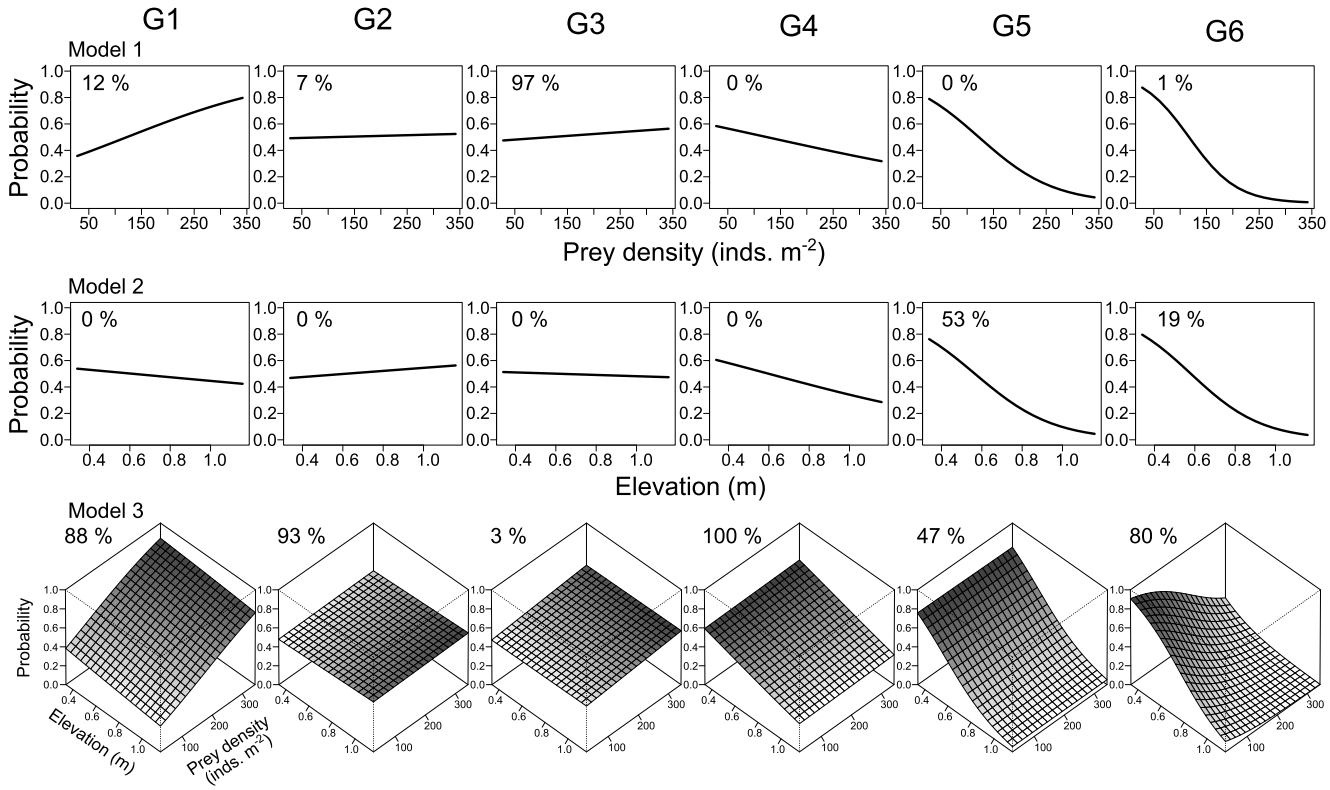

Fig. 8 (Takeuchi and Tamaki, revised)

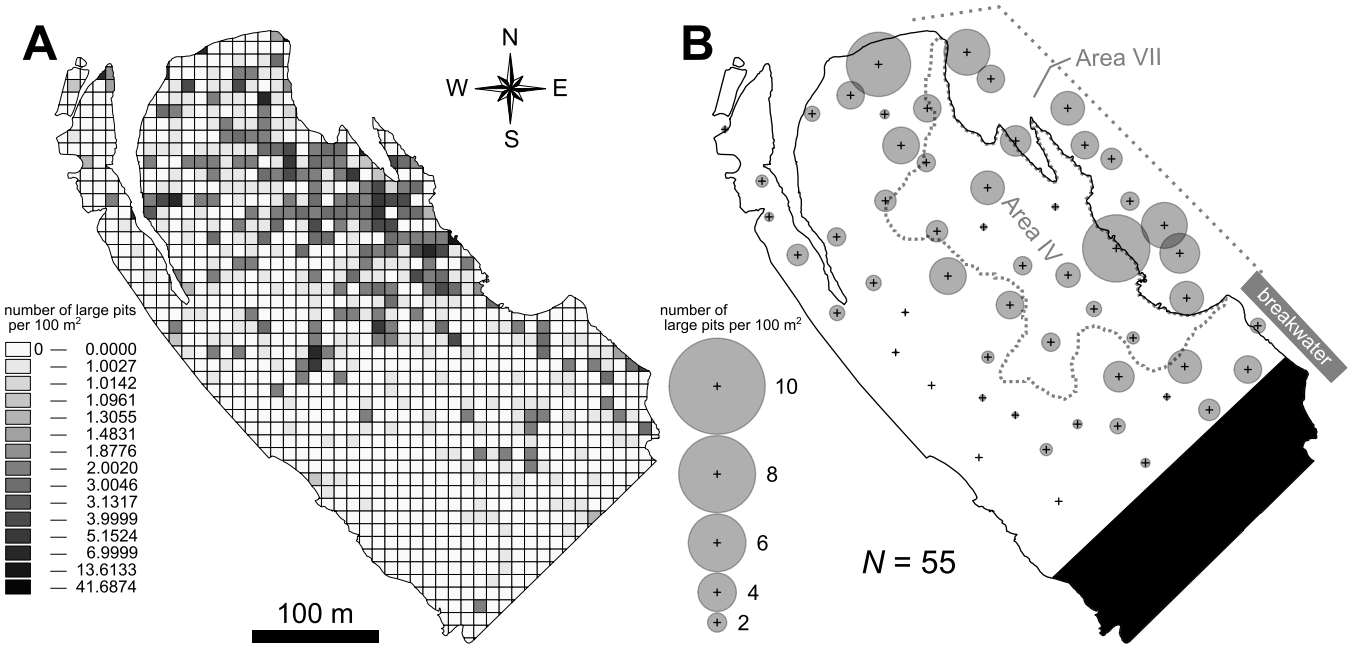

Fig. 9 (Takeuchi and Tamaki, revised)

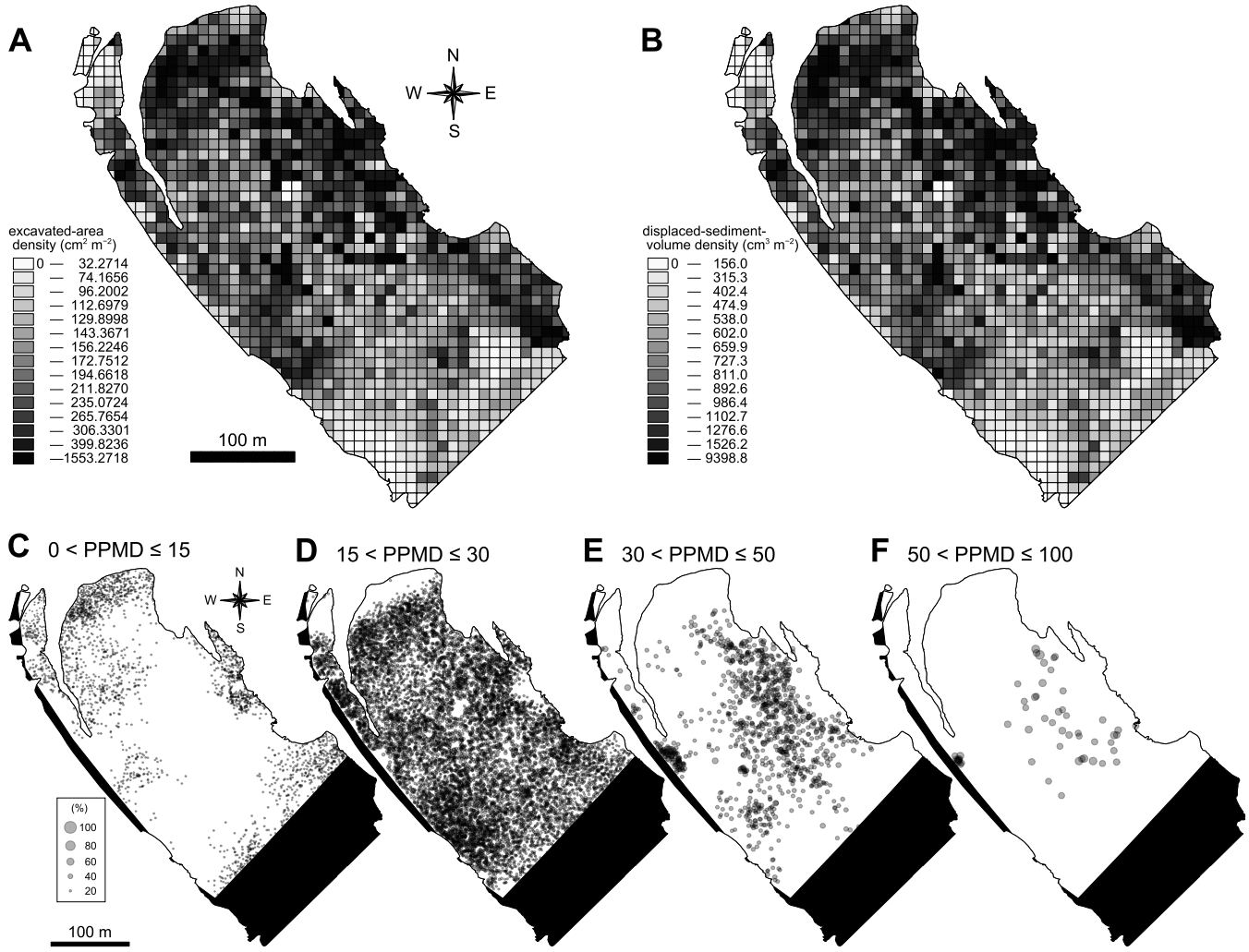

Fig. 10 (Takeuchi and Tamaki, revised)

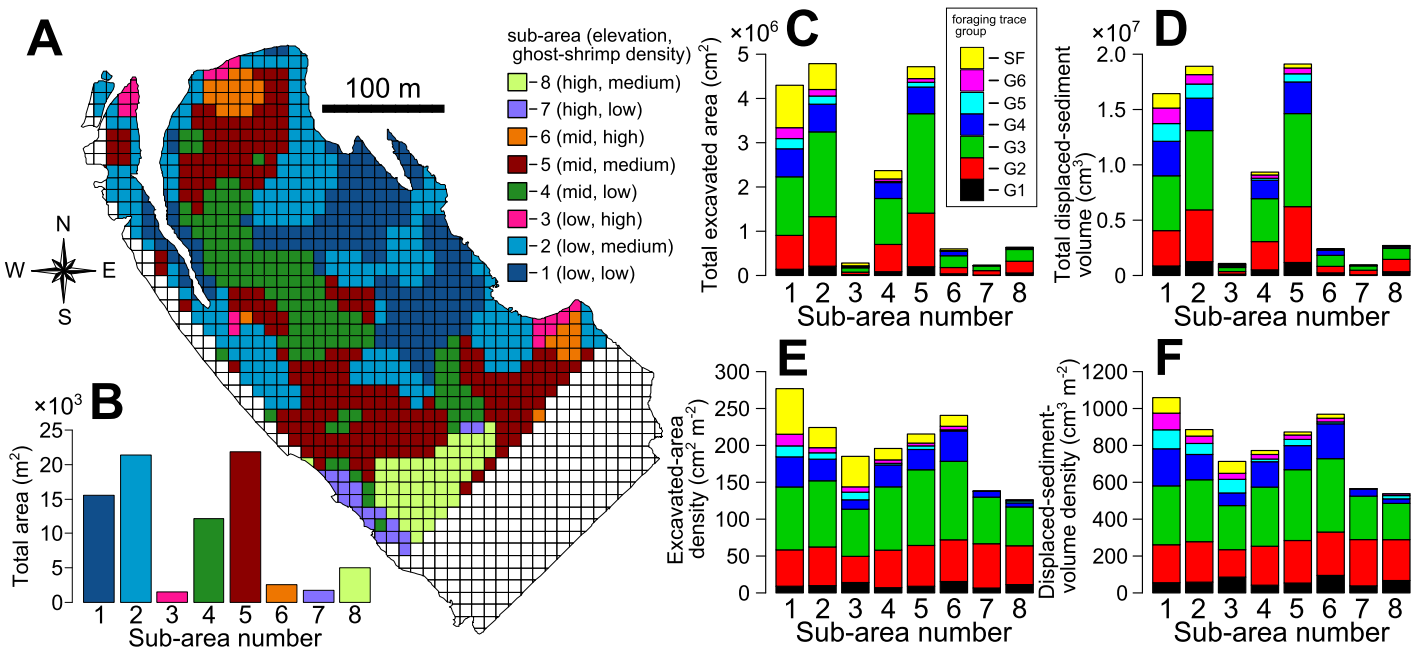

Fig. 11 (Takeuchi and Tamaki, revised)

Table 1. Generalized linear model (GLM) fitting to test for selectivity of stingrays of each size group (G1–G6) for prey (ghost shrimp) density and/or topographic elevation on the Tomioka sandflat. See Fig. 8 for graphic displays. Four models were fit to the binary response variable (1 for the observed points on the sandflat; 0 for the randomly generated points), with prey density alone (Model 1), sandflat elevation alone (Model 2), both (Model 3), and null (= indifferent to both; Model 4) used as explanatory variables, assuming a binomial probability distribution for each. The percentage values in the adoption-rate column for each of G*n*s indicate the occurrence rates as best fit of the 99 runs. For each model, the parameter values in the best-fit linear prediction based on AIC are listed.

Feeding-pit group	Model	Explanatory variable		Linear prediction			Adoption rate (%)
		Ghost shrimp density	Elevation	Intercept	Slope 1	Slope 2	
G1	1	+	–	–0.84	0.01	–	12
	2	–	+	0.38	–0.62	–	0
	3	+	+	–0.59	–0.50	0.01	88
	4	–	–	0.00	–	–	0
G2	1	+	–	0.04	0.00	–	7
	2	–	+	–0.29	0.48	–	0
	3	+	+	–0.11	0.28	0.00	93
	4	–	–	0.00	–	–	0
G3	1	+	–	–0.05	0.00	–	97
	2	–	+	–0.13	0.22	–	0
	3	+	+	–0.06	0.02	0.00	3
	4	–	–	0.00	–	–	0
G4	1	+	–	0.37	0.00	–	0
	2	–	+	1.01	–1.68	–	0
	3	+	+	0.91	–1.15	0.00	100
	4	–	–	0.00	–	–	0
G5	1	+	–	2.00	–0.02	–	0
	2	–	+	2.86	–5.08	–	53
	3	+	+	2.94	–4.82	0.00	47
	4	–	–	0.00	–	–	0
G6	1	+	–	2.96	–0.02	–	1
	2	–	+	2.96	–5.13	–	19
	3	+	+	4.55	–4.78	–0.02	80
	4	–	–	0.00	–	–	0

Table 2. Bioturbation rates about numerical density (ND, numbers m^{-2} d^{-1}), excavated-area density (EAD, cm^2 m^{-2} d^{-1}), and displaced-sediment-volume density (DSVD, cm^3 m^{-2} d^{-1}) for newly-formed pits of rays in estuarine and coastal soft-sediment habitats (all sandflats) from different geographic regions.

Location in geographic region	Intertidal/Subtidal (water depth)	Total census area (number × unit area) (m^2)	Target rays	ND[a]	EAD[a]	DSVD[a]	Reference
South Carolina, U.S.A.	intertidal	300 (3 × 100)	stingray	0.026	57.0	145.0	D'Andrea et al. (2004)[b]
Florida gulf coast, U.S.A.	subtidal (2−3 m)	60	stingray	0.117	91.0	611.1	Reidenauer and Thistle (1981)[c]
same as above	subtidal (NA)	300 (3 × 100)	stingrays	0.082	130.6	NA	Valentine et al. (1994)[c]
innermost Gulf of California, Mexico	intertidal	200−600	bat ray and stingray	0.390	330.5	2883.3	Myrick and Flessa (1996)[e]
off La Jolla, California, U.S.A.	subtidal (17 m)	50	bat ray and stingray	0.148	84.0	420.0	VanBlaricom (1982)[f]
Ningaloo Reef, Western Australia	intertidal	1500 (15 × 100)	stingrays	0.003	11.5	34.5	O'Shea et al. (2012)[g]
Manukau Harbour, New Zealand	intertidal	26866 (38 × 707)	eagle ray	0.004	18.1	180.8	Hines et al. (1997)[h]
same as above	intertidal	724−800	eagle ray	0.028	138.5	1108.2	Thrush et al. (1991)[i]
Amakusa, Kyushu, Japan	intertidal	107516	stingray	0.171	223.0	878.6	this study (sub-areas 1–6)[j]
				0.141	132.1	550.7	this study (sub-areas 7+8)[j]

a–j: see Appendix 3 for descriptions of footnotes.